POLITECNICO DI MILANO

Department of Civil and Environmental Engineering

Master of Science in Energy Engineering

EROSION ESTIMATION OF A GATE VALVE OPERATING IN SAND–WATER FLOW

Supervisor:

PROF. STEFANO MALAVASI

Co-Supervisor:

DR. GIANANDREA MESSA

Master Thesis by: YONGBO WANG

Student ID: 833606

Academic year 2015–2016

Abstract

Gate valve is widely used in oil and gas industry. It is an on/off valve, but sometimes it is also used for regulating the flow. The presence of sand particles in production fluids imposes danger of erosion to gate valve and associated downstream pipe, and may result in failure of valve or leakage from the pipe. In this study, the erosion of a gate valve is numerically investigated to collect preliminary data in view of future experimental testing. Particularly, simplified prototypes of the device, in which the main features of the gate valve in three openings conditions (25 %, 50 % and 75 %) are kept, have been simulated. The standard, most widely used methodology for erosion prediction is employed. That is, first, sand–water two–phase dilute flow is modeled using an Euler–Lagrange numerical approach in a computational fluid dynamics (CFD) simulation software. Afterwards, erosion predictions are made using an embedded utility in a commercial software and an in–house code of the FluidLab research group, which both rely on some semi–empirical erosion models. After validating the fluid dynamic characteristics of the prototypes with respect to experiments in the absence of sand, a sensitivity analysis is made in order to investigate the robustness of the wear estimates upon the different parameters of the erosion prediction model. The numerical simulations indicated that the structure of the particle equation of motion has non–negligible effects on erosion, and that parameters like the restitution coefficients, and the shape of the abrasive particles non–spherical factors are effective as well. Above all, the used erosion model exerts the main influence on the erosion predictions. The work allowed identifying the main features of the erosion process, thereby providing useful information for arranging the experimental campaign.

Keywords: Two–phase flow; gate valve; CFD; impact erosion

Dedication

To my family.

Contents

List of Figures

List of Tables

Chapter 1

Introduction

1.1 Background

In the oil and gas industry, pipes and valves are widely used. During the production stage, oil and gas are recovered to the surface by tubes; at wellhead, choke valves are used to regulate the production rate; then fluids are transported to the separators, storage tanks or refineries through pipes along with many other valves to control the flow rate. As an example, Figure 1.1 shows the separators and pipe connections of Trecate oil field in Northern Italy.

Figure 1.1: Three–phase separators in Trecate oil field

One of the biggest concerns in oil and gas industry is the sand erosion. Sand is usually undesired because, besides decreasing the production level, it may lead even

worse consequences, such as the erosion of pipes and valves in the system. Sometimes, the erosion is so severe that a valve is eroded through or holes are created in pipeline fittings such as T–junctions of elbows. The valve would suffer failure and lose its primary function of regulating and the pipeline faces the danger of leakage, which no doubt imposes very serious problems to production. Therefore, sand control, such as gravel packing, is a common operation in some fields. However, this reduces the concentration of sand in desired fluids but not entirely removes these particles. The damage from sand erosion still exists.

1.2 Impact erosion mechanism

The wear of a component could be caused by abrasion, cavitation, fatigue and stress cracking or impact erosion. In this study, impact erosion is the subject of investigating with the presence of sand particles.

Impact erosion is defined as the removal of material from target walls due to impingement by small solid particles. In their review paper, Parsi et al. [21] summarized that the mechanisms of impact erosion could be divided into two categories. The erosion for brittle material is the result of crack formation: impact of particles cracks the surface in both lateral and radial directions, and further collisions help cracks to grow, eventually small pieces of material are removed (Figure 1.2). For ductile material, Finnie et al. [6] suggested a micro–cutting mechanism: particles that hit the surface at low impact angle creates craters, and with the extension of craters, part of the surface is piled up, thus loss of material occurs (Figure 1.3). Actually, this interpretation is not well accepted by Bellman and Levy [3] though, being inconsistent with the evidence showing that, in ductile material, erosion can occur also at high impingement angles, say, above 40°. Instead, a combined forging–extrusion mechanism was brought through observation of a series of experiments. Of course, the real erosion process is very complex, and probably there is no perfect way to describe it. Furthermore, it may not be rigorous to say that the erosion on a specific material is a result of only one mechanism. This led Forder et al. [7] to the conclusion that the cutting and deformation erosion mechanisms were both presented and the total erosion would be the summation of these two effects.

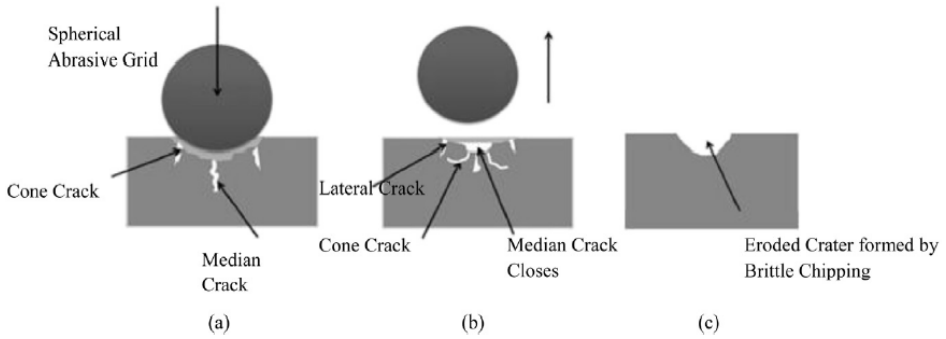

Figure 1.2: Erosion process of brittle material (cited from Parsi et al. [21])

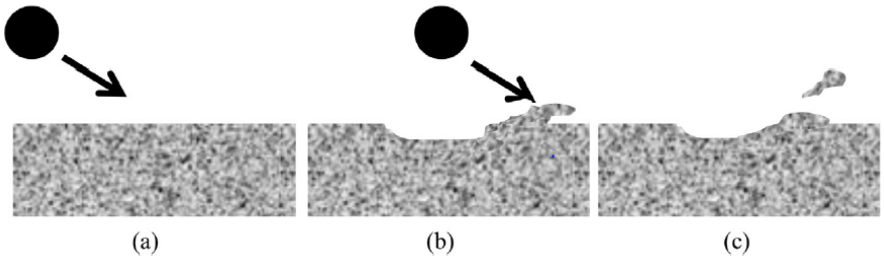

Figure 1.3: Erosion process of ductile material (cited from Parsi et al. [21])

1.3 Erosion–related parameters and brief notes on erosion prediction methods

The severity of impact erosion is evaluated quantitatively by introducing some useful parameters. The first is the erosion rate ($\dot{e}$), which is the mass removal velocity of target material per unit area, the unit is therefore kg/m^2/s. For a selected surface with area A, the integral erosion rate is the mass removal velocity of this specific surface.

$$IE = \int_A \dot{e}\,\mathrm{d}A \tag{1.1}$$

In dimensionless study, the integral erosion ratio (IER) is defined as the ratio between the integral erosion rate and the mass flow rate ($\dot{m}_p$) of injecting particles, which is:

$$IER = \frac{E}{\dot{m}_p} \tag{1.2}$$

Penetration depth (p_d) is a local parameter to quantify the change of wall thickness due to impact erosion. The unit is mm/day and the mathematical formula is:

$$p_d = \frac{\dot{e}}{\rho_t \mathrm{d}A} \tag{1.3}$$

In general, when doing the experiment on a hydraulic device, the device is likely to be destroyed. It makes the experiment study on erosion not economical friendly when considering cost of the equipment purchasing and rig setting up. Therefore, numerical simulation approach has become popular among researchers these years being cost efficient. As early as 1995, Haugen et al. [9] started to use Computational Fluid Dynamics techniques to study the erosion phenomena in a choke valve. Especially with the rapidly increasing of the computational ability, it is possible to simulate complex geometries within reasonable time and limited funding. The most widely used commercial CFD tools, such as Fluent, CFX, Star–CCM+ and Phoenics provide great convenience to run complex simulations. However, one can not neglect that the use of CFD for erosion estimation still have some drawbacks as a result of poor predictive capacity [7, 20, 12, 17, 24, 28]. Uncertainties arising from both the deficiencies in the theoretical basis of the erosion mechanism (see page 2), and the complexity of CFD–based erosion prediction models, which involve many sub–models and parameterizations, are difficult to be defined in practical cases. Therefore, the combination of both numerical study and physical modeling is the a logic and reliable approach. CFD based numerical simulation is actually growing to be quite popular these days. A series of impact erosion studies were performed using this technique, as suggested in section 1.4.

The numerical simulation is divided into two steps, one could refer Njobuenwu and Fairweather [16] in which this methodology applied to pipe bends erosion predictions. These steps are stated briefly as follows:

1. Firstly, solve the continuous phase flow with RANS turbulence models employed, and the aim is to have a flow field that is independent to the computational domains so that the effects on erosion prediction from unstable flow field can be minimized;

2. Next step is the particles tracking and erosion prediction:

   (a) Inject the sand particles and make trajectories in the continuous flow simulated in the first step. Motions of particles are solved using Discrete Phase Model (DPM), and impacting information (including impact speed, impact angle, impact locations, etc) is known and recorded;

   (b) Apply semi–empirical erosion models to make the predictions on materials losses. In these models, erosion rate, erosion ratio and penetration depth can be calculated once the materials properties and impacting information

are supplied.

1.4 Previous studies

It is worth effort devoting to the study of erosion for the benefit of reducing losses in oil and gas industry. The main purpose in erosion study is to understand at where the erosion tends to happen in pipes and valves, and how badly the effects are, which will give us some ideas about the reliability of the equipment and probably provide the correct directions to make some improvements on valve design or pipe coatings to enhance their erosion resistance. Many related investigations have been done in the last few decades and certainly having contributed the erosion study a lot recently.

Real geometries can turn out to be very complicated, thus are not easy to be studied directly. Simplified geometries, instead, while maintaining the major features of complex valves, reduce the efforts and expenses in both numerical studies and experimental tests. In the case of pipelines, elbows, straight tubes or T–junctions are modeled; for valves, a partially opened valve can be modeled as an obstacle inside of a pipe, for example. It is noticed that the choke valve is mostly studied, probably due to its vital existence when regulating flow in oil or gas field.

1.4.1 Elbows and other pipeline components

McLaury et al. [13] studied both the straight pipe and elbow. The erosion on elbow was a result of direct impingement while the erosion on straight pipe was due to random impingement mechanism. The author developed a mechanistic model to predict the percentage of particles that travels through the sublayer–buffer region and finally impact the wall. And the agreement between this model with an existing general model was quite good whenever the fluid phase was air or water. Wood et al. [28] used the erosion model proposed by Bitter–Hashish to predict the erosion in a straight pipe and bend by a mixture of sand–water at 10 vol%. Erosion locations were carefully examined. It was found in the straight pipe, the maximum erosion was distributed to either side of the pipe bore; in the bend, wear was more significant in the base and in the outer. Also, the prediction was reported to agree with experimental measurements. An intense comparison study on the dilute air–sand two phase flow in plugged tee and elbow was done by Chen et al. [4], from which it was concluded that sand loading affected the erosion greatly, erosion in both plugged tee and elbow was reduced under high sand loading, likely due to the non negligible particle–particle interactions, as

explained by the author; and erosion of plugged tee was lower when two phase flow was air–sand but it became higher than erosion of elbow in term of water–sand flow according to the CFD simulations, revealed the significant effect from fluid properties. Zhang et al. [29] from University of Tulsa compared the particle velocities and erosion in air and water flows from computed results to measured data. Simulation predicted the particle impact velocities well compared with direct impact test; erosion by E/CRC (from [29]) and Oka models [19, 18] were verified as reliable and accurate ways to make predictions in some cases. Wong et al. [27] in the erosion experiments on an aluminum plate with a hole suggested rapid rounding of the sharp edges of the hole, which, however, not reflected in the CFD simulation. It was considered as a reason for the underestimation of the erosion rate in computational study.

1.4.2 Choke valve

In an oil field, a choke valve is located between the production well and the separator, with primary function as controlling the oil production level. The choke valve is exposed to a harsh environment with raw oil flowing through it. Impact erosion from sand particles is expected. While the choke valve is so important to a filed that the erosion characteristics are well studied. In Figure 1.4, a cage and sleeve choke valve is presented.

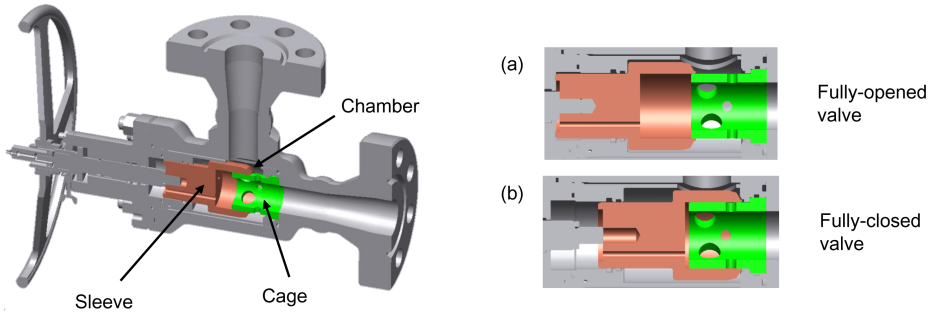

Figure 1.4: Cage and sleeve choke valve
(a)when the valve is fully opened; (b)when the valve is fully closed

Forder et al. [7] studied the erosion of sand particles in a choke valve by implementing an erosion prediction utility in the CFX code. With the aid of experimental data of direct impact tests, the constants of erosion models that are depended on types of materials were calibrated, thus increasing the reliability of the erosion predictions of the valve. It was concluded that one order of magnitude reduction in erosion rate could be achieved by properly changing the design of the choke valve. Paggiaro et al. [20] from

GE Oil&Gas also chose a CFD model to predict the sand erosion in choke valves. The predicted and measured dissipation characteristics of the device were in good agreement, whilst the erosion rates were seriously underestimated. However, the locations where erosion phenomenon was significant were consistent with the experiments. Wallace et al. [24] decided to firstly simulated a simple geometry as a representative of a choke valve and then moved to the more complex geometry. The dissipation characteristics of both devices were predicted reasonably well, and the erosion rates were under-predicted, just like the above case. In the simple geometry, erosion rates from simulation were 60% lower than experimental data; in valve geometry, the erosion rates by experiments were 10–15 times higher than numerical predictions. In order to optimize the lifespan of a choke valve, Haugen et al. [9] examined the erosion severity of 28 different materials by means of direct impact tests. By interpolating the experimental data, specific values of constants in an empirical erosion equations for each material were obtained and it was reported that the longevity of the choke valve could be largely extended by carefully selecting the proper material when manufacturing. In the article of Nøkleberg and Søntvedt [17], an early version of Fluent was used to simulate the air–sand two phase flow and make wear estimates. The geometry was a choke valve with four different openings: 10%, 12.5%, 25% and 50%, and the first 3 openings were under erosion investigation while the 50% opening was just used for flow field study. It was found that the commercial CFD software was satisfactory when used to compute the flow field through the choke valve. Regarding the erosion rates prediction, it gave 2 or 3 times lower than the lab test, and, by the authors' opinion, that could be considered as a very good result for the very complicated geometry.

1.4.3 Gate valve & related studies

An horizontal gate valve works by lowering down a rectangular gate with a cylindrical hole in it to stop the fluid through, and when it is lifted, the fluid is able to pass by without any restrictions. Figure 1.5 shows the geometry of a half–opened gate valve used in this study.

Unlike choke valves, interests from researchers to gate valve studies are limited, although gate valve appears to be everywhere in industry. The reason could be that, being traditionally designed as an on/off valve, a gate valve is either fully opened or totally closed. And in the former case, it would be easier to model it as a part of joint pipes or a cavity. This is what Lin et al. [12] did in a numerical study on a fully opened gate valve. The erosion prediction models were validated by experimental data

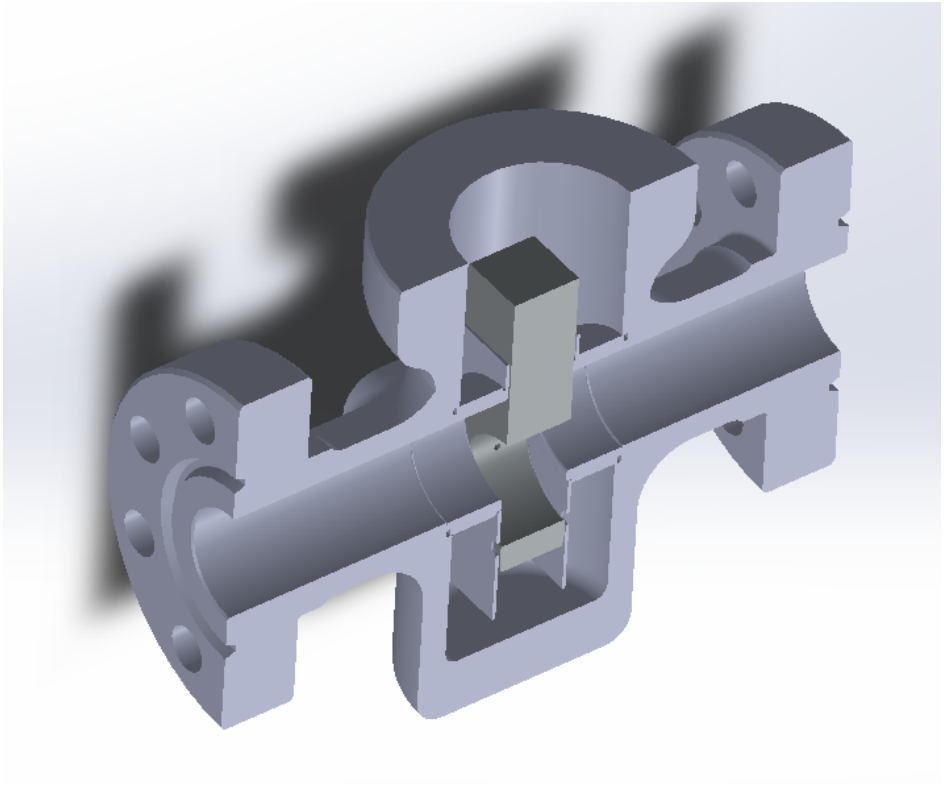

Figure 1.5: Gate valve at 50% opening

in a pipe and an elbow. Prediction on erosion distributions on the geometry was as expected. Parameters like cavity width, particle diameter and inlet velocity affected the total erosion ratio in different manners. The authors even proposed an empirical yet quite simple formula with the 3 variables mentioned above to estimate the total erosion ratio. Finally, Wheeler and Wood [25] did some experiments to compare the erosion resistance of various kinds of coatings on a gate valve and found that the HVOF coatings' superior performance was due to the higher hardness compared to sand particles.

1.5 Scope of this thesis

Since the studies of erosion on gate valves are very few at present, it would be a good idea to fill in the blank by doing some preliminary research on this subject. An additional reason is that there are actually people from oil and gas industry using the gate valve as a control valve. Those gate valves are operated at different openings to regulate the flow rates. So it is also meaningful to study the erosion phenomena in a partially opened gate valve.

In this study, numerical simulation is chosen to study the erosion on a gate valve and prototypes as simplified version of this device at different openings. The fluid dynamic behavior of both the valve and the prototypes will be tested in a flow loop in the Hydraulic Laboratory of Politecnico di Milano, and the CFD results of this study will be employed to preliminarily define the conditions to be tested in the experiments.

The approach applied in this study is similar to the ones used in a paper of Wallace et al. [24]. A simplified prototype with 25%, 50% and 75% openings is studies first; then the investigation on a more complicated gate valve with these 3 openings follows. Well designed experiments are used to validate numerical simulations.

Chapter 2

Methodology

The primary task before making the erosion predictions in a numerical way is to solve the multiphase flow field. The multiphase flow here is sand–water two phase flow, with sand concentration being very low.

There are two approaches to describe a multiphase flow field, namely, Eulerian–Eulerian and Eulerian–Lagrangian. The Eulerian–Eulerian model, also known as two fluid model, treats each phase as a continuous phase and a set of continuity and momentum equations for each phase are solved. The coupling between two phases is done by taking care of inter–facial exchange forces due to mass, momentum and energy transfer. Another widely used model is Discrete Phase Model (DPM), based on the Euler–Lagrange approach. The fluid phase is seen as a continuum and Navier–Stokes equations (or, most frequently, variants such as RANS or LES) are needed to determine the flow field; conversely, the dispersed phase, consisting of sand particles, is solved by tracking a large number of particles.

This approach is practically applicable if the sand concentration is sufficiently low that the particle–particle interactions are negligible, so the tracking procedure can be performed without significant computational cost. This assumption is definitely met here. Moreover, in our simulations, the fluid phase can hardly be disturbed by the solid phase, also due to the low volume fraction of the dispersed phase. With the hypothesis that sand particles trajectories would not affect the continuous phase (or, in other words, one–way coupling), computational burden would be reduced considerably, as one can always firstly simulate the single phase (water) flow, then track sand particles through DPM, and finally adopt an erosion model to make predictions.

As having already been mentioned in the previous chapter, the CFD–based methodology for erosion prediction involves two steps in sequence, namely the simulation of the liquid–particle flow, and the application of a single–particle erosion model. In the

particle tracking procedure, physical particles are grouped to be parcels, which are acting as the computational particles. In this thesis, the term "parcels" is equivalent to the term "particles".

2.1 Governing equations in the two–phase flow

2.1.1 Equations for the liquid phase

The continuous phase is water, and under the one–way coupling assumption, the governing equations are the same as single phase flow. The mass conservation equation and momentum equation for continuous phase are expressed as follows:

Continuity equation:

$$\frac{\partial \rho}{\partial t} + \nabla \cdot (\rho \mathbf{u}) = 0 \tag{2.1}$$

Momentum equation:

$$\frac{\partial (\rho \mathbf{u})}{\partial t} + \nabla \cdot (\rho \mathbf{u}\mathbf{u}) = \rho \mathbf{g} - \nabla P + \nabla \cdot \mu \nabla \mathbf{u} \tag{2.2}$$

In equations (2.1) (2.2), $\mathbf{u}$ is the fluid velocity; t is time; ρ is the fluid density; P is the pressure; $\mathbf{g}$ is the gravity acceleration constant and μ is the fluid dynamic viscosity.

2.1.2 Solving the continuous phase

The behavior of laminar flow could be described by directly solving standard Navier–Stokes equation. Contradictorily, for turbulent flow (in our case), predicting the flow velocity is extremely time consuming due to the random feature of turbulence. Nevertheless, a time averaged formula of the Navier–Stokes equation, referred to as the Reynolds–Averaged Navier–Stokes (RANS) equation can be a good alternative. The basic idea is that flow velocity is expressed as the summation of mean velocity and velocity fluctuation, as shown in (2.3):

$$\mathbf{u} = \mathbf{U} + \mathbf{u}' \tag{2.3}$$

where, $\mathbf{U}$ is the fluid mean velocity and $\mathbf{u}'$ is the velocity fluctuation.

Compared to the Navier–Stokes equations, the RANS contains extra term associated to the correlations between the fluctuating velocity components and Reynolds stresses, requiring additional equations as closures for this model. Some models account for the Reynolds stresses by introducing eddy viscosity term. Among them, the

standard k–ε model is the most widely used and validated turbulence model for industrial applications. k represents the turbulent kinetic energy per unit mass and ε is the energy dissipation rate per unit volume. They are solve in conjunction with an algebraic equation for μ_t, turbulence viscosity.

$$\frac{\partial(\rho k)}{\partial t} + div(\rho k \mathbf{U}) = div\left[\frac{\mu_t}{\sigma_t} grad(k)\right] - \rho\varepsilon + 2\mu_t S_{ij} \cdot S_{ij} \tag{2.4a}$$

$$\frac{\partial(\rho \varepsilon)}{\partial t} + div(\rho \varepsilon \mathbf{U}) = div\left[\frac{\mu_t}{\sigma_\varepsilon} grad(\varepsilon)\right] - C_{2\varepsilon}\rho\frac{\varepsilon^2}{k} + C_{1\varepsilon}\frac{\varepsilon}{k} 2\mu_t S_{ij} \cdot S_{ij} \tag{2.4b}$$

$$\mu_t = C_\mu \rho \frac{k^2}{\varepsilon} \tag{2.4c}$$

Where, the constants are: $C_\mu = 0.09$; $\sigma_k = 1.00$; $\sigma_\varepsilon = 1.30$; $C_{1\varepsilon} = 1.44$; $C_{2\varepsilon} = 1.92$; and S_{ij} is the average rate of deformation.

In order to investigate the sensitivity of the numerical results with respect to the turbulence models, the Realizable k–ε model is also applied in this study considering its better performance for separated or recirculated flow. Further discussions are available in the following chapter.

2.1.3 Equations for the solid particles

The motion of particles is influenced by interacting with continuous phase. The trajectory of each particle is obtained by the integration of Newton's second law, and the forces that are taken into account are drag force F_D, virtual mass force $\mathbf{F}_V$, pressure gradient force $\mathbf{F}_P$, gravity and buoyancy $\mathbf{F}_G$ and lift force $\mathbf{F}_L$. The momentum equation of the dispersed phase is:

$$m_p \frac{\mathrm{d}\mathbf{u}_p}{\mathrm{d}t} = \mathbf{F}_D + \mathbf{F}_V + \mathbf{F}_P + \mathbf{F}_G + \mathbf{F}_L \tag{2.5}$$

Where, m_p is the mass of the injecting particles. The term $\mathbf{F}_D$ is drag force, and it is generated by the velocity difference between the solid phase ($\mathbf{u_p}$) and the fluid phase ($\mathbf{u}$), which affects the movement of particles significantly. And it is evaluated by Equation (2.6):

$$\mathbf{F}_D = m_p \frac{18\mu}{\rho_p {d_p}^2} \frac{C_D Re_p}{24} (\mathbf{u} - \mathbf{u}_p) \tag{2.6}$$

Where, ρ_p is the particle density, d_p is the particle diameter, C_D is the drag coefficient. For non–spherical particles, the drag coefficient is calculated by the equation (2.7) developed by Haider and Levenspiel [8]:

$$C_D = \frac{24}{Re_p}\left(1 + b_1 {Re_{p_2}}^{b}\right) + \frac{b_3 Re_p}{b_4 + Re_p} \tag{2.7}$$

Where

$$b_1 = exp(2.3288 - 6.4581\phi + 2.4486\phi^2) \tag{2.8a}$$

$$b_2 = 0.0964 + 0.5565\phi \tag{2.8b}$$

$$b_3 = exp(4.905 - 13.8944\phi + 18.4222\phi^2 - 10.2599\phi^3) \tag{2.8c}$$

$$b_4 = exp(1.4681 + 12.2584\phi - 20.7322\phi^2 + 15.8855\phi^3) \tag{2.8d}$$

And ϕ is the shape factor, the ratio of the surface area of a sphere having the same volume as the particle and the actual area of the particle; and Re_p is relative Reynolds number, defined as:

$$Re_p = \frac{\rho d_p |\mathbf{u} - \mathbf{u}_p|}{\mu} \tag{2.9}$$

The virtual mass force, also known as added mass force, reflects the force required to accelerate the mass of the surrounding continuous phase near a dispersed phase particle. It is needed to be considered when the density of the continuous phase is not too small compared to the density of dispersed phase. It is usually neglected in gas–solid flows but considered important in gas–liquid flows. The significance of virtual mass force in sand–water flows is yet unclear, thus needed to be evaluated by sensitivity analysis.

$$\mathbf{F}_V = m_p C_V \frac{1}{2} \frac{\rho}{\rho_p} \frac{\mathrm{d}(\mathbf{u} - \mathbf{u}_p)}{\mathrm{d}t} \tag{2.10}$$

Where, C_V is the virtual mass coefficient, which is 0.5 as commonly reported in the literature.

The liquid pressure is not uniform around particles, hence affecting their motion. A pressure gradient force is introduced to account for this effect. Like virtual mass force, when the density of the fluid is much lower than the density of the particles, the pressure gradient force becomes negligible. However, the importance of this force is not well understood in liquid–solid flows.

$$\mathbf{F}_P = m_p \frac{\rho}{\rho_p} \mathbf{u}_p \nabla \mathbf{u} \tag{2.11}$$

Gravity and buoyancy would influence the distribution of particles, making the concentration of sand particles higher in the lower part of pipes. The force that is responsible for this effect, is:

$$\mathbf{F}_G = m_p \mathbf{g} \frac{(\rho_p - \rho)}{\rho_p} \tag{2.12}$$

The lift force is due to both shear and particle rotation. In particular, Saffman's lift force is due to shear at small relative Reynolds number [1], which is not exactly the

case of the flows considered in this study. According to Mei [14] the lift force is more appropriately expressed in Equation 2.13:

$$\mathbf{F}_L = J^* \cdot 3.0844 \frac{m_p}{\rho_p d_p} \sqrt{\frac{\nu}{|\omega|}} (\omega \times (\mathbf{u} - \mathbf{u}_p)) \tag{2.13}$$

Where, ν is the kinematic viscosity of fluid phase; ω is the unhindered fluid vorticity; J^* is a function of Re_p:

$$J^* = \begin{cases} (1 - 0.3314\sqrt{\beta}) exp(\frac{-Re_p}{10}) + 0.3314\sqrt{\beta}, & \text{if } Re_p \leq 40 \\ 0.0524\sqrt{\beta Re_p}, & \text{if } Re_p > 40 \end{cases} \tag{2.14}$$

Where,

$$\beta = \frac{\sqrt{2\boldsymbol{D} : \boldsymbol{D}}}{|\mathbf{u} - \mathbf{u}_p|} d_p \tag{2.15}$$

And the $\boldsymbol{D}$ is the strain rate tensor of the fluid.

2.1.4 Effect of restitution coefficients

One of the peculiar features of the Lagrangian description of the particles is their interactions with solid walls. When a particle hits the wall, its total kinetic energy will decrease, because some kinetic energy from the particle is transferred to the wall. The difference between particle velocity after and before impact is expressed by means of two restitution coefficients, defined as velocity ratios in normal ($\mathbf{n}$) and tangential ($\mathbf{t}$) directions.

$$e_n = \frac{u_{pnA}}{u_{pnB}} \tag{2.16a}$$

$$e_t = \frac{u_{ptA}}{u_{ptB}} \tag{2.16b}$$

Where subscript A means "after impact", B means "before impact". To evaluate the effects of restitution coefficients on wear estimations, three options have been considered.

Unit coefficients

Ideally, for a perfect collision, no kinetic energy loss thus the restitution coefficients are unit, i.e.:

$$e_n = 1 \tag{2.17a}$$

$$e_t = 1 \tag{2.17b}$$

Forder correlation

Forder et al. [7] found a relationship between restitution coefficients and impact angle, and gave a set of equations:

$$e_n = 0.988 - 0.78\alpha + 0.19\alpha^2 - 0.024\alpha^3 + 0.027\alpha^4 \tag{2.18a}$$

$$e_t = 1 - 0.78\alpha + 0.84\alpha^2 - 0.21\alpha^3 + 0.028\alpha^4 - 0.022\alpha^5 \tag{2.18b}$$

The correlation (Equation (2.18)) is for AISI 4130 steel, and when the target material is changed, the coefficients may change.

Grant& Tabakoff correlation

The expression has been proposed by Grant and Tabakoff in 1975 [21] based on experiments on aluminum 2024. The expression is:

$$e_n = 0.993 - 1.76\alpha + 1.56\alpha^2 - 0.49\alpha^3 \tag{2.19a}$$

$$e_t = 1 - 2.12\alpha + 3.0775\alpha^2 - 1.1\alpha^3 \tag{2.19b}$$

2.2 Erosion models

Once the single phase flow is simulated and the particles are tracked using DPM, the erosion prediction can then be made by applying the erosion models.

As mentioned before, erosion is affected by many factors, including target materials, particle size, particle shape, impact velocity and impact angle, etc. An erosion model quantifies these dependencies for a single particle hitting a surface. Typically, the general form of an erosion model is:

$$ER = K \cdot |\mathbf{u}_{p,i}|^n \cdot f(\alpha) \tag{2.20}$$

Where, ER is the erosion ratio, namely the ratio between the mass of material removed by the particle and the mass of the particle; K is a constant depending on the particle and target material properties; $\mathbf{u}_{p,i}$ is the particle impact velocity, n is the exponent for velocity, values may vary from 1.6 to 2.6 [21]; and $f(\alpha)$ is a function of impact angle. The type of target material (ductile or brittle, see section 1.2) has great effect on this angle function. And the angle functions ($f(\alpha)$) can be very different for ductile and brittle materials, as indicated by Figure 2.1 (cited from DNV [5]).

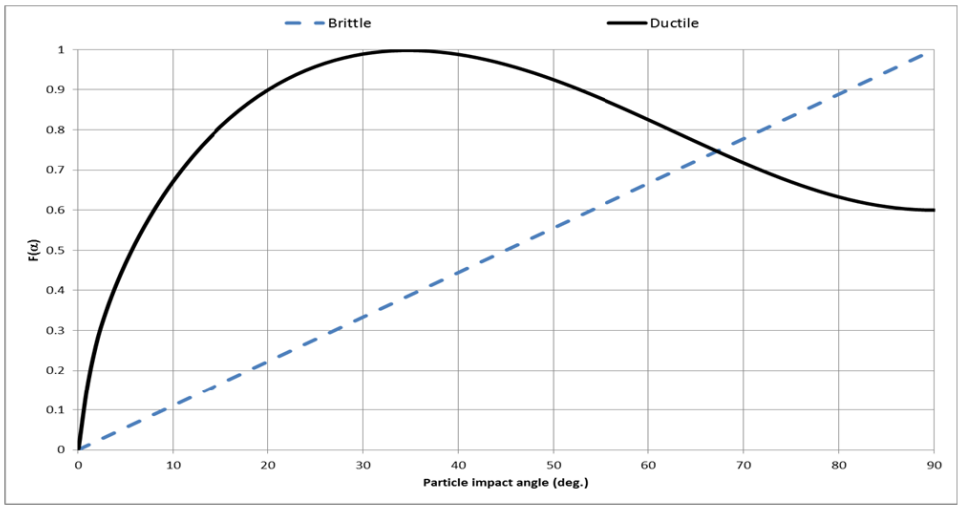

Figure 2.1: Impact angle functions for brittle and ductile materials

In order to quantify the influence from erosion models on wear estimations, which proved to be a significant consideration in the simulation of abrasive jet impingement tests[15], three well developed correlations have been included in this thesis.

The E/CRC model (see, for instance, Zhang et al. [29]) takes account for the hardness of target material, particle shape, impact velocity and angle.

$$ER = K(BH)^{-0.59} F_s |\mathbf{u}_{p,i}|^n f(\alpha) \tag{2.21}$$

Where,

$$f(\alpha) = 5.4\alpha - 10.11\alpha^2 + 10.93\alpha^3 - 6.33\alpha^4 + 1.42\alpha^5 \tag{2.22}$$

And BH is the Brinell hardness of target material; F_s is the particle shape coefficient, with $F_s = 0.2$ for round particle, $F_s = 0.53$ for semi–rounded particle, $F_s = 1.0$ for angular particle; $K = 2.17 \times 10^{-7}$ and $n = 2.41$, are all constants which were derived from experiments where sand particles were directly impacting wall made of Inconel 718 .

Another model, developed by Oka et al.[19, 18], includes the effect of particle size. And the velocity exponent is not considered as a constant. The formulas are:

$$ER = f(\alpha) ER_{90} \tag{2.23}$$

Where

$$ER_{90} = 10^{-9} \rho_t K (aHv)^{k_1 b} \left(\frac{|\mathbf{u}_{p,i}|}{u'} \right)^{k_2} \left(\frac{d_p}{d'} \right)^{k_3} \tag{2.24}$$

And

$$f(\alpha) = (\sin(\alpha))^{n_1} (1 + Hv(1 - \sin(\alpha)))^{n_2} \tag{2.25}$$

In these equations, ER_{90} is the erosion ratio when particles impacting wall at the normal angle; ρ_t is the density of target material; Hv is the Vickers number of target material; u'=104 m/s and d' = 326 µm are the reference values for particle impact velocity and diameter respectively. when impacting particles are sand, $K = 65$, $k_1 = -0.12$,$k_3 = 0.19$, while n_1,n_2 and k_2 are relevant to the Hv, with the following correlations:

$$n_1 = 0.71(Hv)^{0.14} \tag{2.26a}$$

$$n_2 = 2.4(Hv)^{-0.94} \tag{2.26b}$$

$$k_2 = 2.3(Hv)^{0.038} \tag{2.26c}$$

DNV–GL [5] from Norway proposed a sand erosion model with the possibility of being applied to a variety of target materials. The general equation is:

$$ER = K \cdot |\mathbf{u}_{p,i}|^n \cdot f(\alpha) \tag{2.27}$$

With

$$f(\alpha) = A \cdot [\sin(\alpha) + B(\sin(\alpha) - \sin(\alpha)^2)]^k \cdot [1 - exp(-C \cdot \alpha)] \tag{2.28}$$

Where constants, $A = 0.6$,$B = 7.2$,$C = 20$,$k = 0.6$ are for ductile materials. In this study, the target materials are aluminum and AISI304, accordingly, the values of constants are presented in Table 2.1:

Table 2.1: Values of K and n in DNV–GL model

	K	n
Aluminum	5.8×10^{-9}	2.3
AISI304	2.0×10^{-9}	2.6

Chapter 3

Single–phase fluid dynamic characterization

In this chapter, the continuous phase flow is simulated to obtain single–phase predictions that are independent to the grids of the prototypes and the gate valve with 3 different openings. Moreover, the sensitivity of two turbulence models, namely k–ε model and Realizable k–ε model, are studied. Besides, the results from simulations are compared with those from experiments.

3.1 Description of the simulated geometries

As previously introduced, the scope of this study is to numerically investigate the impact erosion in a gate valve in view of future experimental tests. However, the destructive nature of experiments and high cost of the real device lead to the decision of testing simplified prototypes of the device first. The valve is inserted in a pipe with a diameter of 81 mm, and the thickness of the gate is 49.4 mm, jointed by a valve body which is in total 473 mm long. The prototype is an obstruction with a flange, which reproduces the intersection of the gate at different openings and the pipe. Particularly, three prototypes have been designed, corresponding to valve openings of 25%, 50% and 75%. Figure 3.1 shows a prototype with a flange that simulates the gate valve at 50% opening. And Figure 3.2 is the geometry of the gate in the gate valve.

The fluid dynamic behavior of the valve and prototypes is provided making reference to the flow coefficient that is introduced by the IEC standard [10] to quantify their dissipation characteristics. The flow coefficient is defined in Equation (3.1):

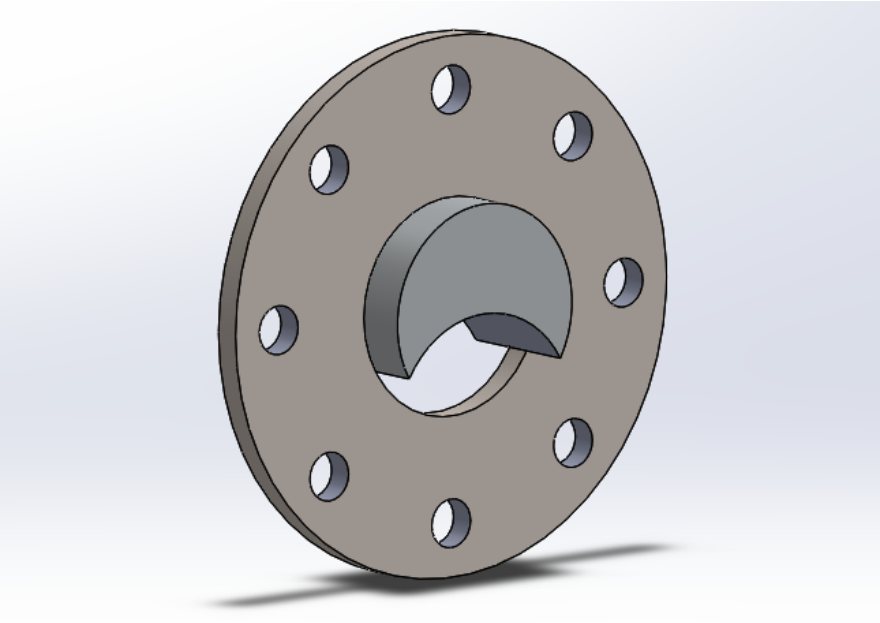

Figure 3.1: Prototype that corresponds to the gate valve at 50% opening

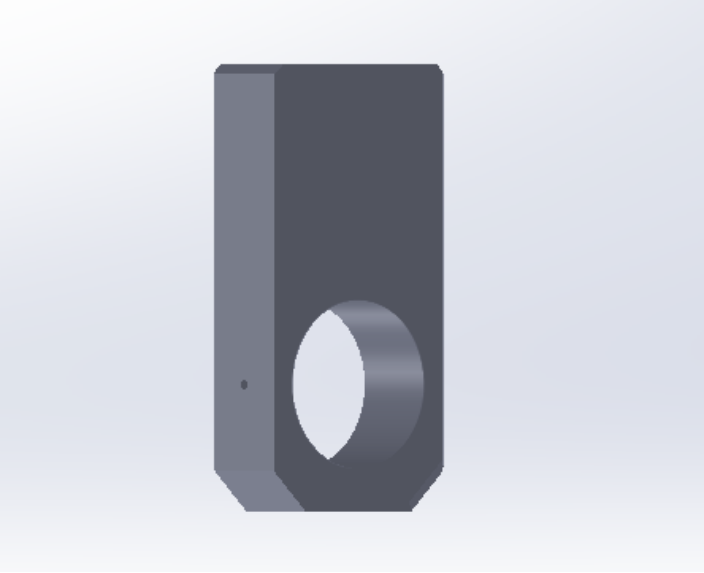

Figure 3.2: The gate in the gate valve

$$C_v = Q\sqrt{\frac{SG}{P_1 - P_2}} \tag{3.1}$$

Where: Q is the flow rate, in gpm (gallon per minute); SG is the ratio between the actual fluid density and the density of water in 20°; P_1, P_2 are pressures measured $2D$ upstream and $6D$ downstream the device respectively, in psi (calculated as the pressure integral of the cross section area); C_v is flow coefficient, in gpm/$\sqrt{\text{psi}}$.

3.2 Fluid domain, boundary conditions, and other numerical settings

The fluid domain has been obtained from the solid geometries by Solidworks. In particular, the fluid domain for the valve is shown in Figure 3.3

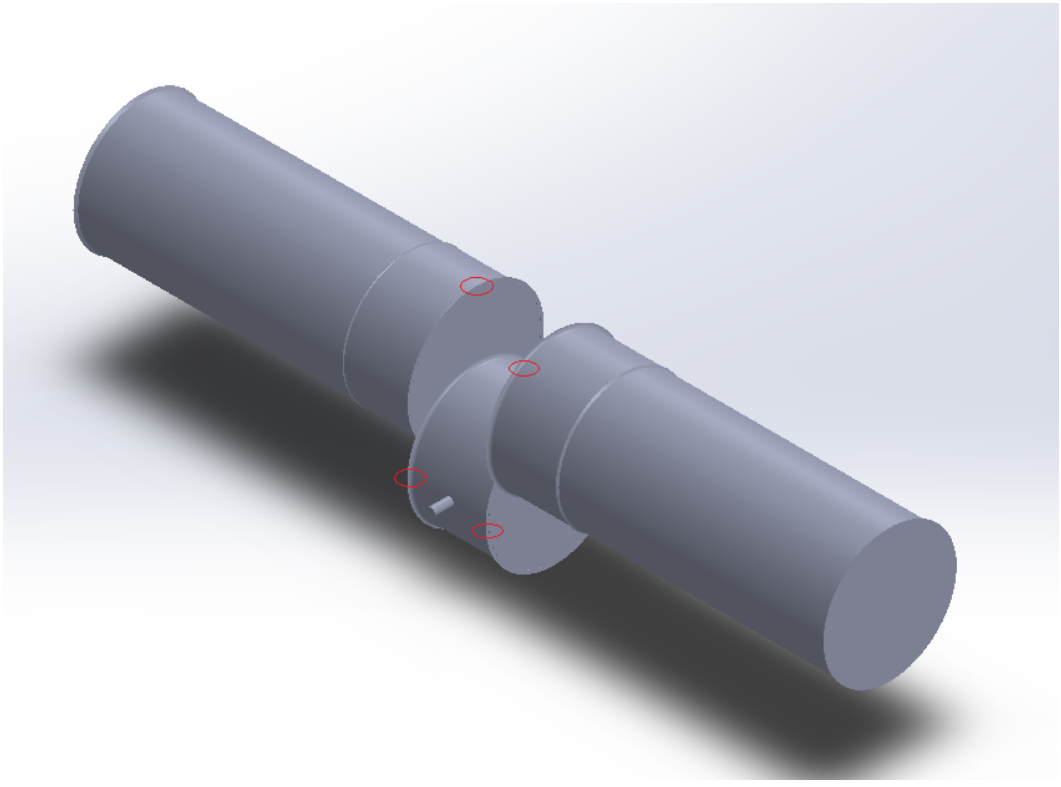

Figure 3.3: Fluid domain of the valve at 50% opening

Note that in the actual simulations, the chamfers marked in the figure were removed because they prevented from generating high quality meshes and this further caused divergence problem during iterations. The fluid domains of three prototypes have been created in a similar way, and they consist of a block and parts of pipes on both sides. These fluid domains (as shown in Figure 3.4) are also created in Solidworks.

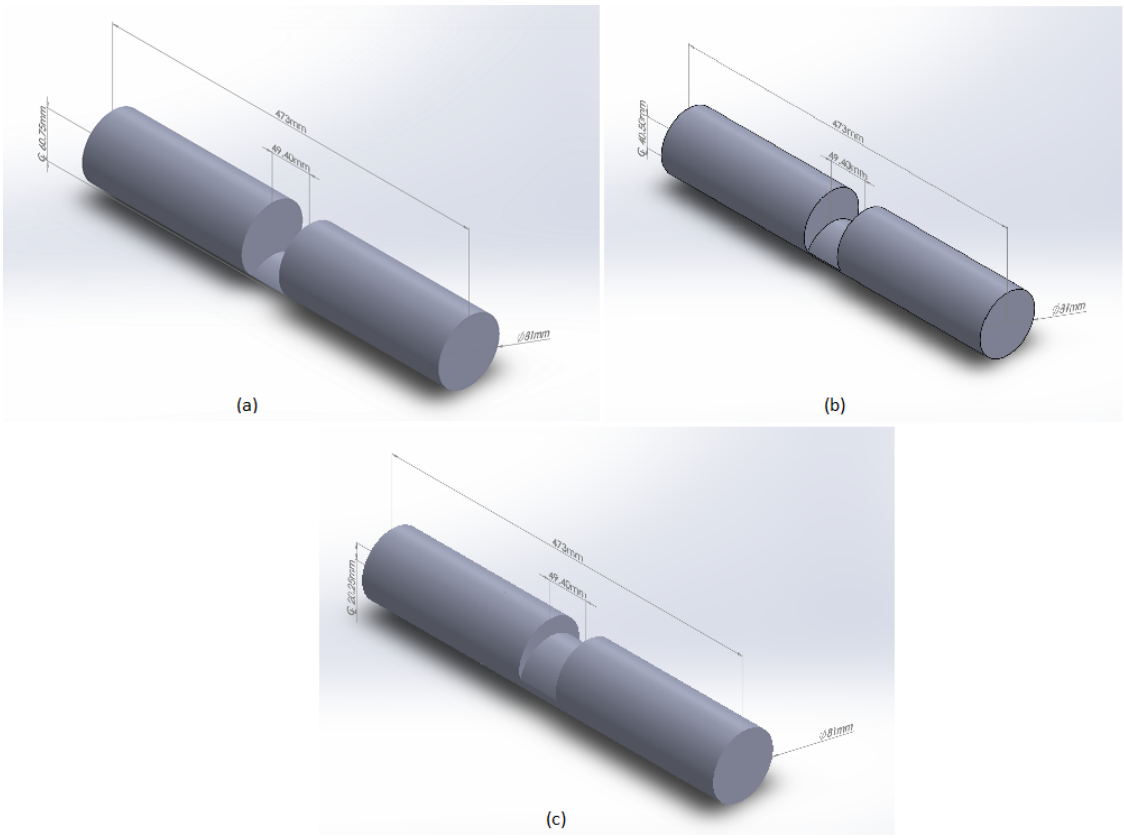

Figure 3.4: Fluid domain of the prototype with (a)25% opening; (b)50% opening and (c)75% opening

The geometries depicted in the figures above are referred as "valve region", as they correspond to the actual length of the valve body (473 mm). This has been done in order to provide valves of erosion which are easily related to the real device. Upstream pipe and downstream pipe are added to the valve region. The fluid entering into the upstream pipe has a uniform velocity profile. However, due to the effect of viscous forces, flow velocity near the wall decreases while flow velocity far away from the wall increase. A fully developed flow is achieved when the velocity profile does not change after reaching to a certain location in the pipe. The distance between the entrance (or the location where the flow is distorted) and a point where the flow becomes fully developed is called entry length. As an example, Figure 3.5, taken from White [26], shows the developing laminar flow in a straight pipe.

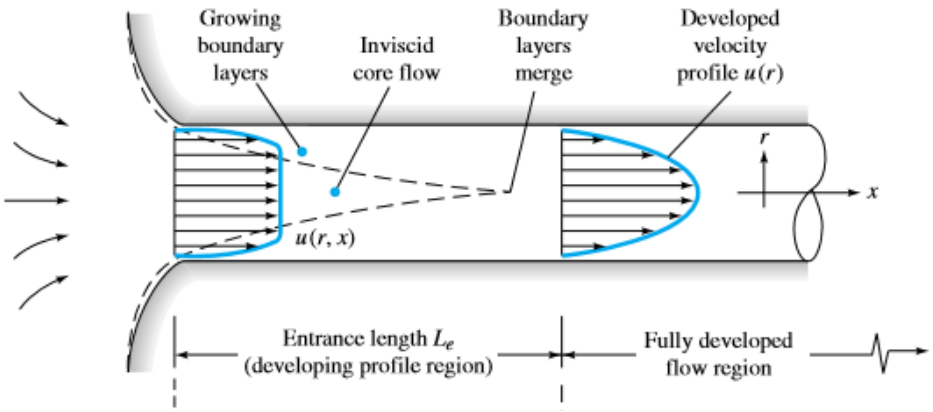

Figure 3.5: Fully developed laminar flow in a pipe

Flow which is not fully developed is practically non reproducible, and inconsistent with the future experiments. For this reason, fully developed flow is desired in the pipe before and after the valve region. So the length of upstream pipe and downstream pipe should be decided by this criterion.

In order to have fully developed flow, it was suggested to install at least a upstream pipe $30D$ long and a downstream pipe $20D$ long according to Wallace[24], where D is the diameter of the pipe. In a paper by Lien et al. [11], a minimum entry length of $130h$ was required in a channel with a hydraulic diameter of $D_h = 1.84h$, where h is the height of the channel. Hence the entry length was around $70D$ for a highly turbulent flow. An empirical formula for turbulent flow entry length estimation in a smooth pipe is: $L \approx 4.4Re^{1/6}D$ (cited from Stelian [23]), yielding approximately an entry length of $38D$.

The carrier fluid considered in the simulations is water at 20° with density and

viscosity are $\rho = 998.2$ kg/m^3 and $\mu = 0.001003$ Pa $\cdot$ s respectively. The mean velocity at the inlet section is $u_m = 5.0$ m/s, resulting in a pipe Reynolds number, Re, equals to 403060 (the pipe diameter, D, is 81 mm). Notice that it is much larger than 2300, indicting the flow is fully turbulent.

With the purpose of reducing the already high computational burden in the liquid–particle flow simulations, it is necessary to find the minimum length of upstream pipe and downstream pipe ensuring the flow is fully developed. So, a straight pipe geometry $100D$ long was created and meshed. The pipe flow was then simulated in Fluent. Axial velocity profiles were derived at different axial locations and the axial velocity changes along the center line was also presented, as shown in Figure 3.6 and Figure 3.7.

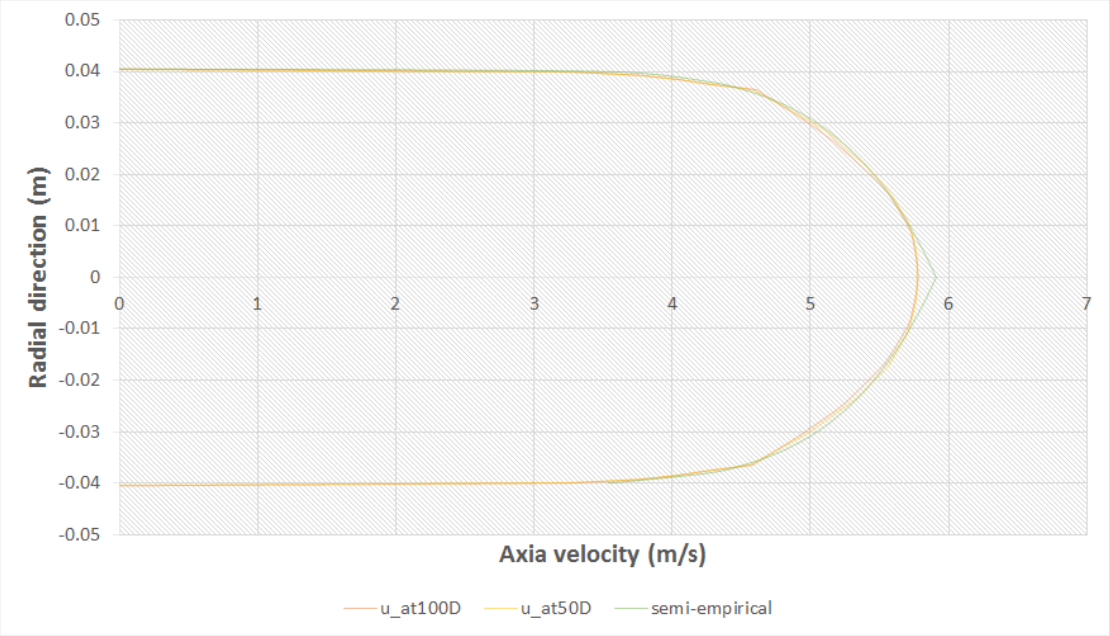

Figure 3.6: Comparison of velocity profiles at $L = 50D$ and $L = 100D$

In Figure 3.6, the label *semi-empirical* is a correlation of velocity profile for a fully developed turbulence flow in smooth pipes, cited from Schlichting [22]. The axial velocity profile at $L = 50D$ is very similar to the axial velocity profile at $L = 100D$; and it also matches the velocity profile predicted from the correlation very well. Besides, the axial velocity variation is negligible starting from $L = 50D$, proving that the a length of $50D$ is sufficient for fully developed turbulent flow. Therefore, $50D$ upstream straight pipe and 50 downstream straight pipe were assembled with the valve region, forming the actual fluid domain.

The type of imposed boundary conditions is the same for all test cases. At the inlet section, a velocity of 5 m/s was supplied normal to the boundary, and the values

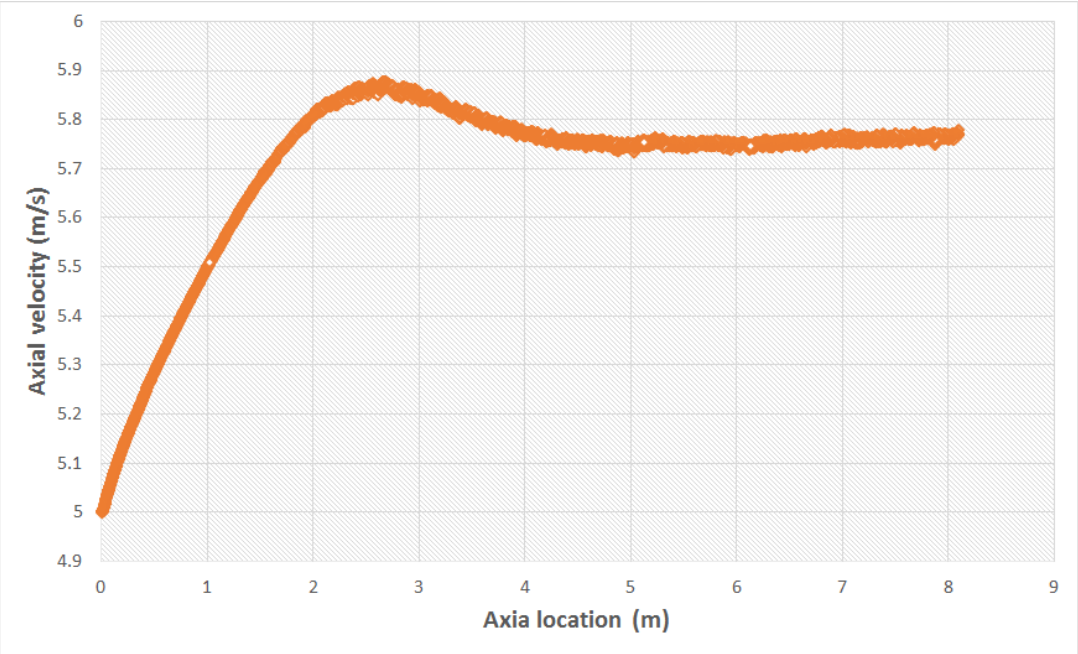

Figure 3.7: Velocity changes along the center axial of the pipe

of k and ε were obtained from turbulence intensity, $I = 3.2\%$, which is calculated by an empirical correlations described in Fluent User Guide [2]: $I = 0.16(Re)^{-1/8}$, with $Re = 403060$. At the outlet section, the gauge pressure was set to 0. Over all the solid walls, the wall function approach was applied. Wall functions are a set of semi–empirical formulas to bridge the viscosity–affected region between the wall and the fully–turbulent region. For standard wall function, to guarantee the accuracy and reliability of the solutions, dimensionless y^+ should be in the range from 11 to several hundred. Accordingly, the inflation layer settings in Ansys Workbench were adjusted with caution. The first layer thickness was set to 0.3 mm, corresponding to $y^+ \approx 30$, the number of layers was 8 and growth rate was set to 1.2.

As mentioned before, two turbulence models have been employed, and they are standard k–ε and realizable k–ε. This was done to investigate the effect of the turbulence model on CFD estimates. Other numerical settings in Fluent are as follows. The Solver was set to Pressure–based, Steady State; The SIMPLE was chosen as Pressure–Velocity Coupling scheme; in Spatial Discretization settings, the Gradient followed Least Squares Cell Based rule, Pressure setting was in the Second Order, while other variables were set to Second Order Upwind. The rest of settings were kept default.

3.3 Grid independence study and effect of turbulence model

In this study, the goal of grid sensitivity study is to have the flow coefficient calculated independent of the number of computational cells. For each turbulence model adopted, a grid independence study was performed. Thus, the turbulence model sensitivity was analyzed.

The fluid domains described in Section 3.2 are imported into Ansys Meshing, and several coarse to fine tetrahedral meshes were generated. It is noted that the inflation setting was applied to all solid walls to reach the requirements of the standard wall functions. Qualities of meshes were checked to make sure that no convergence problem occurred in numerical simulations.

3.3.1 Results of prototypes

Nine different meshes have been created for the 50% opening prototype. These meshes were read in Fluent, proper settings were imposed before simulations. During simulation, scaled residuals were monitored as convergence criteria. In general, all residuals reached 10^{-6} before simulation being stopped. However, for fine meshes with many computational cells, the simulations were considered finished when all residuals reduced to about 2×10^{-5}. The flow coefficient of the prototype with 50% opening with respect to the number of cells is reported in Table 3.1 and The plot is presented in Figure 3.8.

Table 3.1: Flow coefficient of the prototype at 50% opening

Number of cells	C_v (Standard)	C_v (Realizable)
0.7×10^6	119.6	
1.1×10^6	118.5	
1.3×10^6	121.1	
2.6×10^6	121.9	
4.5×10^6	123.6	114.4
5.7×10^6	123.7	
6.5×10^6	123.8	114.3
7.5×10^6	124.9	
8.6×10^6	123.6	114.2

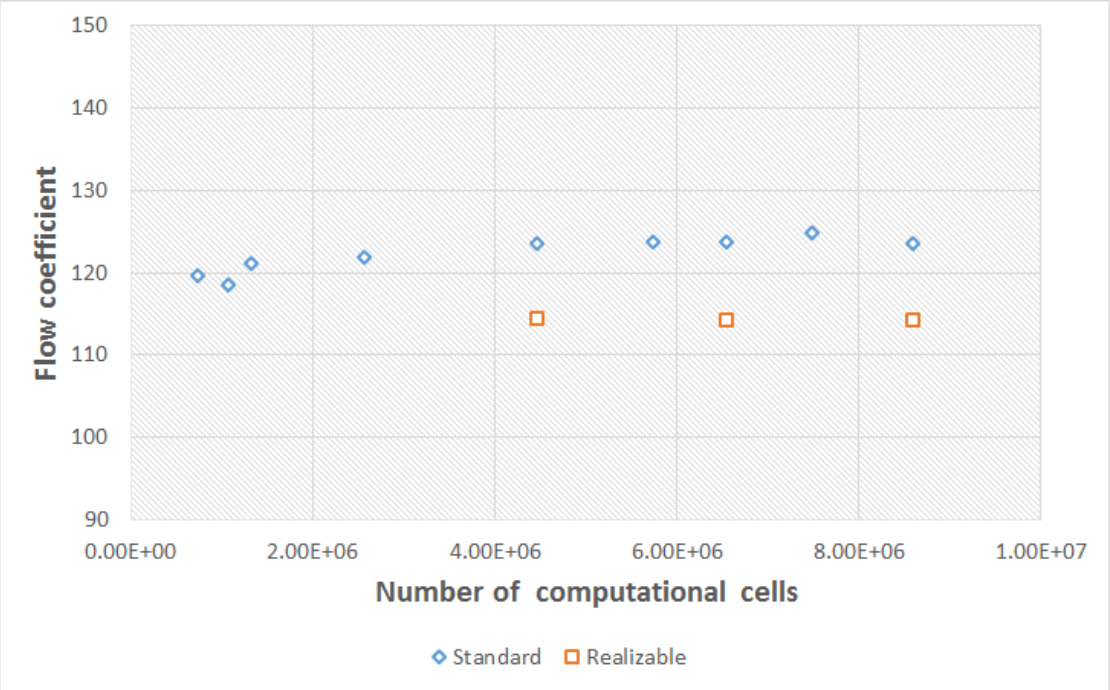

Figure 3.8: Grid independence analysis on the prototype at 50% opening

In both table and figure, "Standard" represents Standard k–ε model; "Realizable" represents Realizable k–ε model.

The flow coefficient becomes relatively stable when the number of computational cells reaches 4.5 million, suggesting to consider meshes with the number of cells equal to or higher than 4.5 million. By changing the turbulence model from the Standard k–ε to Realizable k–ε, the flow coefficient estimates remain grid–independent, but the values were around 8% lower.

Using the same approach, flow coefficients of the prototypes at 25% opening and 75% opening were calculated. In order to reduce the computational time, the number of computational cells starts from around 5 million. Results are reported as follows:

Table 3.2: Flow coefficient of the prototype at 25% opening

Number of cells	C_v (Standard)	C_v (Realizable)
5.0×10^6	35.97	35.47
6.3×10^6	36.06	35.41
7.7×10^6	36.19	35.58
9.0×10^6	34.71	35.78

Except for the simulations of the prototype at 25% opening, when using the Standard k–ε model, where a sudden decrease of the flow coefficient was observed, C_v

Table 3.3: Flow coefficient of the prototype at 75% opening

Number of cells	C_v (Standard)	C_v (Realizable)
5.1×10^6	322.1	312.7
6.4×10^6	323.8	315.6
7.7×10^6	324.7	316.8
9.3×10^6	327.2	315.9

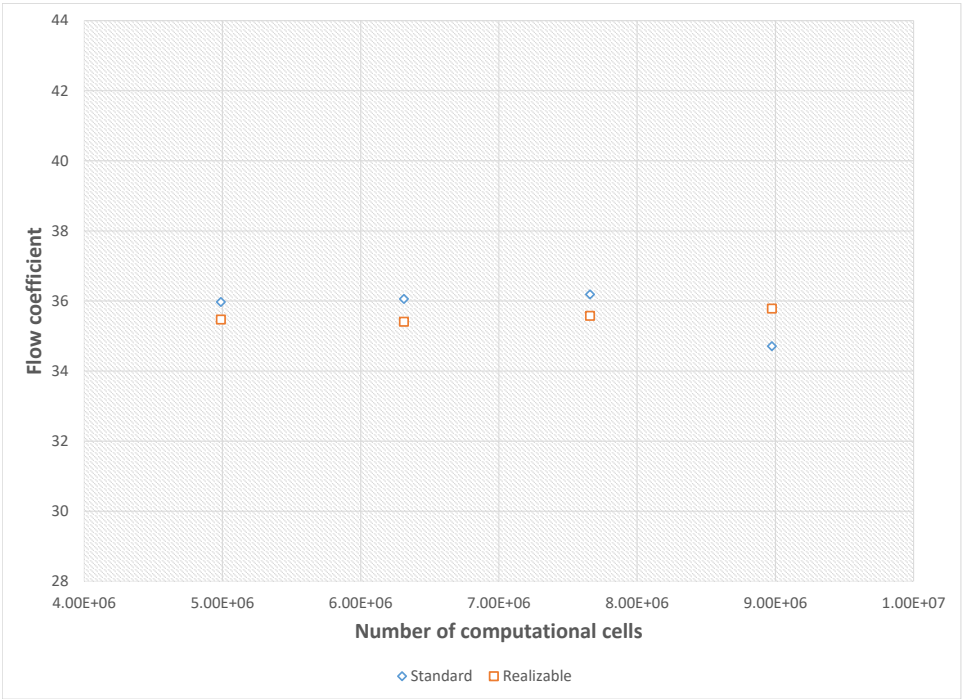

Figure 3.9: Grid independence analysis on the prototype at 25% opening

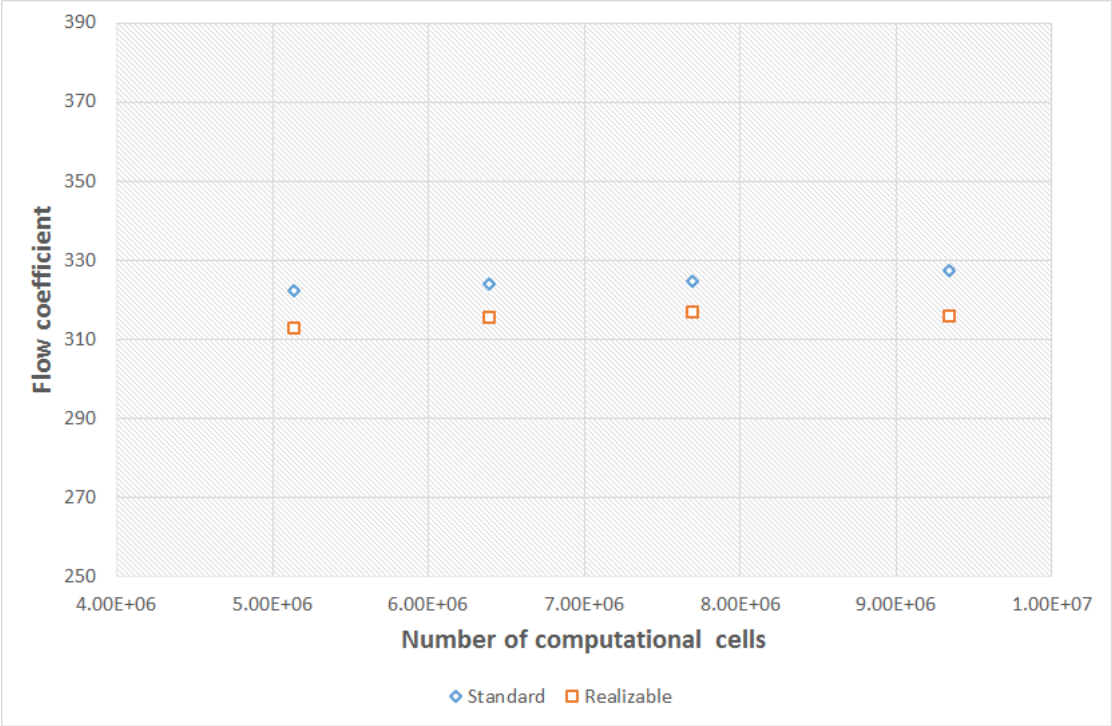

Figure 3.10: Grid independence analysis on the prototype at 75% opening

remains essentially independent for all the other cases study. The possible explanation for this strange behavior could be the convergence of the domain with 9.0 million cells was not entirely fulfilled, thus the flow coefficient of this domain was not convincing. Changing the turbulence models leads the differences in predictions, however, the variation is within 3% and 4% for 25% and 75% opening prototype respectively.

3.3.2 Results of gate valve

The geometry of the gate valve as well as the computational domain and the main numerical settings have already been illustrated. Different computational grids were generated and the inflation settings followed the rule applied to the prototypes. In all cases, the number of cells was above 4 million, as suggested in prototype study. Flow coefficients are presented in Table 3.4, Table 3.5 and Table 3.6. The grid independence can be concluded in Figure 3.11 to Figure 3.13.

From the tables and figures above, it is found that the flow coefficient predictions on meshes with 4 or 5 million cells are becoming relatively stable. Moreover, compared with the flow coefficients calculated in prototypes, the flow coefficients of the gate valve are less sensitive to the two turbulence models.

The flow coefficients calculated in the prototypes and in the gate valve using stan-

Table 3.4: Flow coefficient of the gate valve at 25% opening

Number of cells	C_v (Standard)	C_v (Realizable)
4.3×10^6	29.92	29.71
6.4×10^6	30.30	30.01
8.4×10^6	30.21	29.90

Table 3.5: Flow coefficient of the gate valve at 50% opening

Number of cells	C_v (Standard)	C_v (Realizable)
4.9×10^6	102.5	103.1
6.3×10^6	102.4	102.8
8.3×10^6	102.5	102.9

Table 3.6: Flow coefficient of the gate valve at 75% opening

Number of cells	C_v (Standard)	C_v (Realizable)
5.8×10^6	299.7	292.4
6.9×10^6	299.8	292.2
8.9×10^6	302.5	293.9
9.3×10^6	301.2	293.4

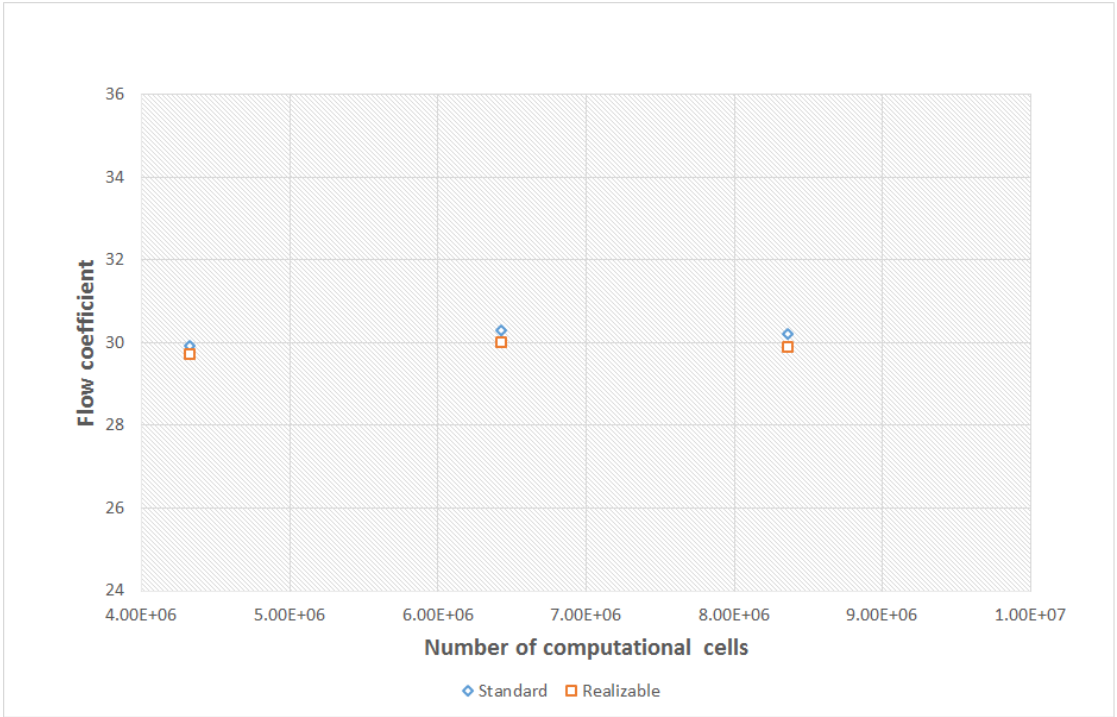

Figure 3.11: Grid independence analysis on the gate valve at 25% opening

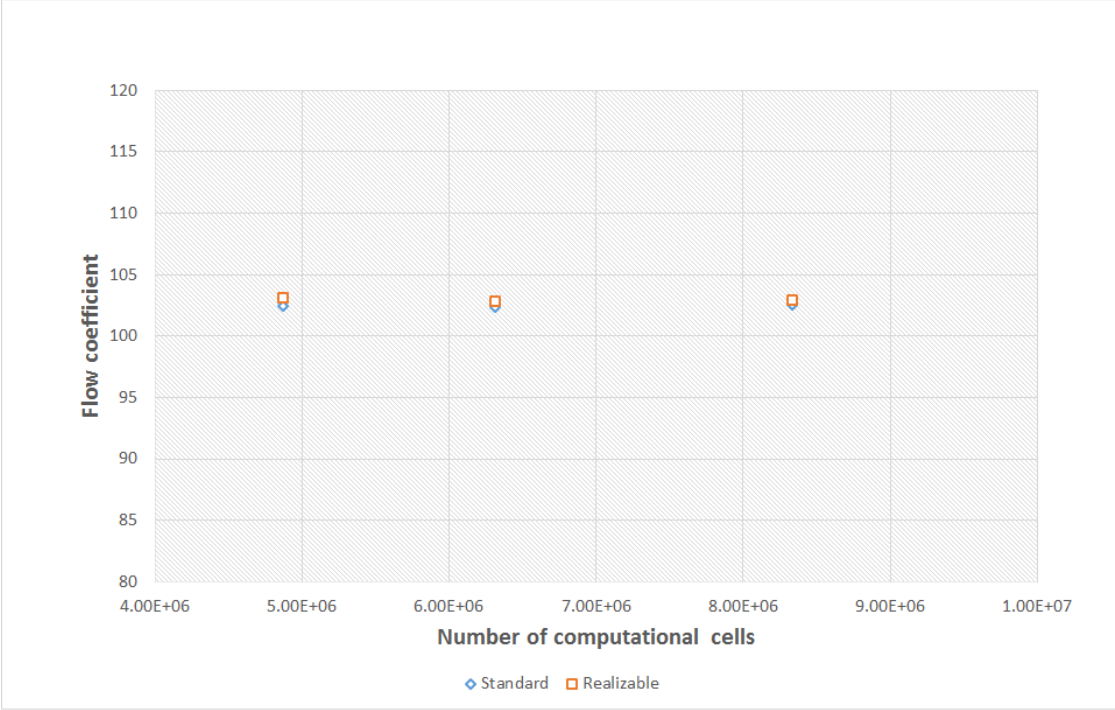

Figure 3.12: Grid independence analysis on the gate valve at 50% opening

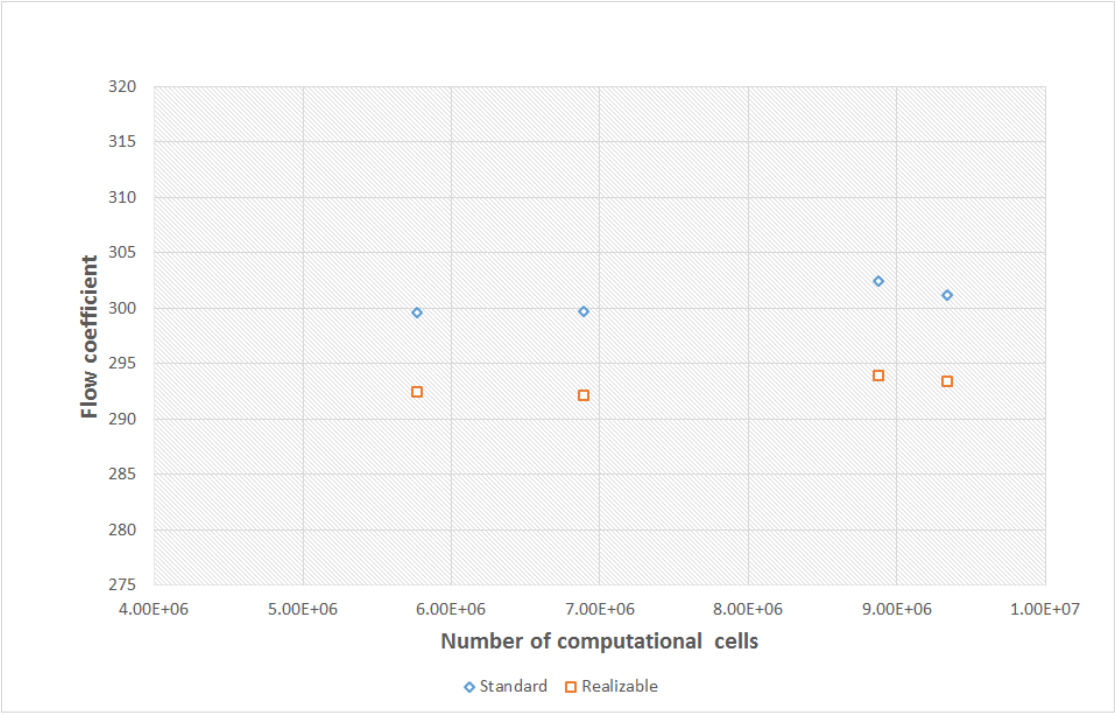

Figure 3.13: Grid independence analysis on the gate valve at 75% opening

dard k–ε model are compared in Figure 3.14.

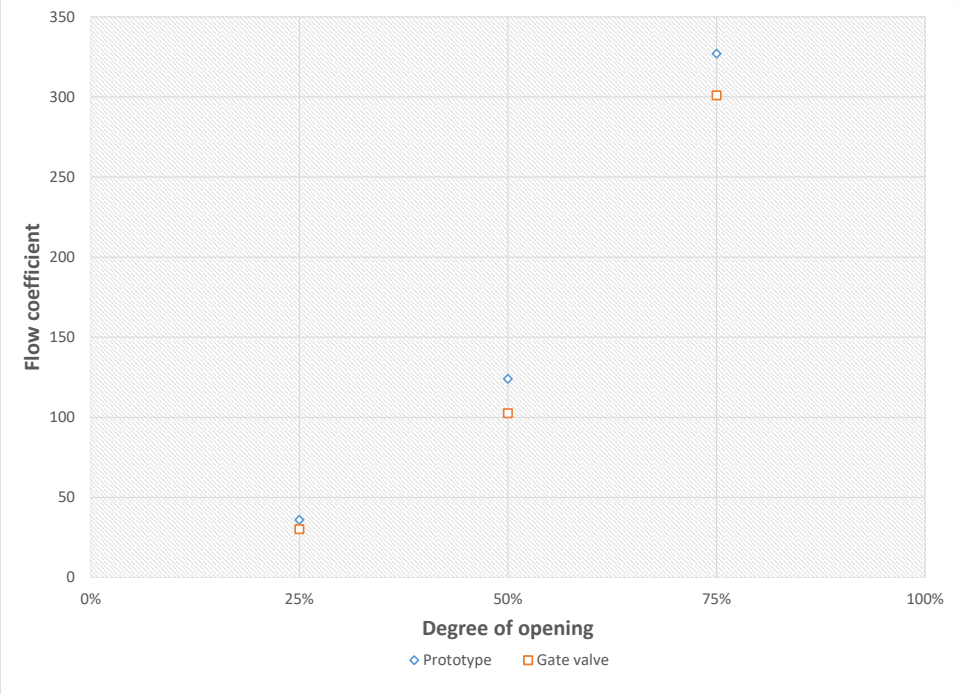

Figure 3.14: Comparison of flow coefficients in prototypes and in gate valve using k–ε standard model in simulation

The flow coefficients obtained in all prototypes are lower than the predictions made in the gate valve at all three openings. The maximum difference is about 25% as indicated in 50% opening case. This is assumed to be caused by the different structures between these two geometries.

3.4 Comparison against experiments

The flow coefficients obtained in experiments performed by the FluidLab research group are reported in Table 3.7.

Thus, the comparisons between experimental data and simulations are indicated in Figure 3.15 and Figure 3.16.

It is found that for both the prototypes and the gate valve at three openings, the flow coefficients are underestimated in predictions. Compared with the predictions in the prototypes, the numerical results of the gate valve have a better match to

Table 3.7: Flow coefficients from experiments

Degree of opening	C_v of prototype	C_v of gate valve
25%	43.5	31.1
50%	151.5	118.3
75%	477	296.8

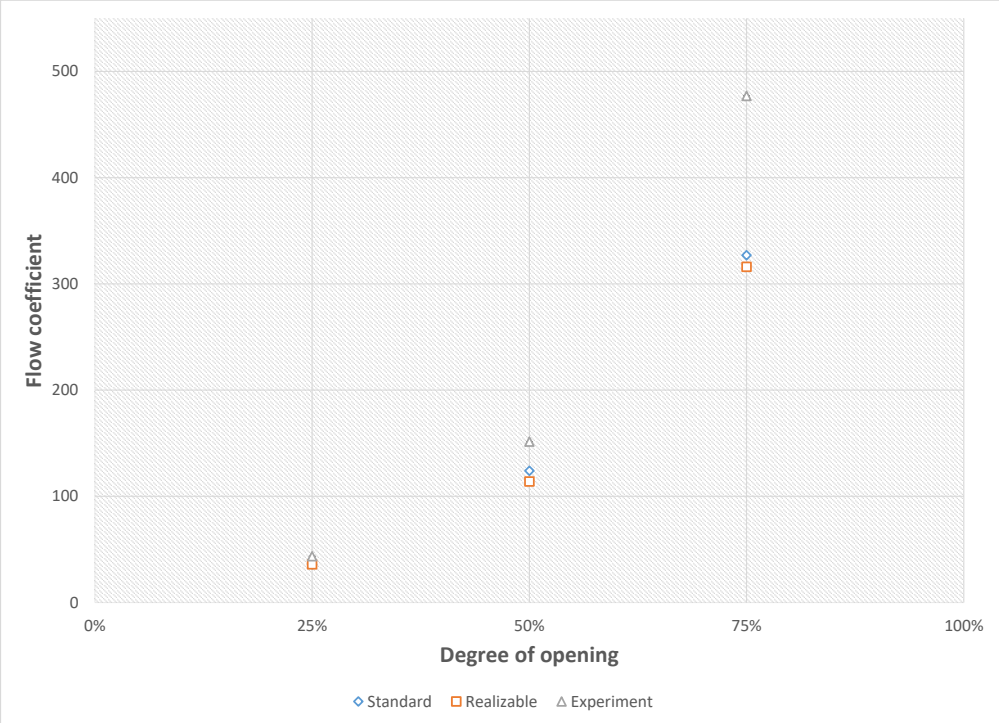

Figure 3.15: Flow coefficients comparison between simulations and experiments of prototypes

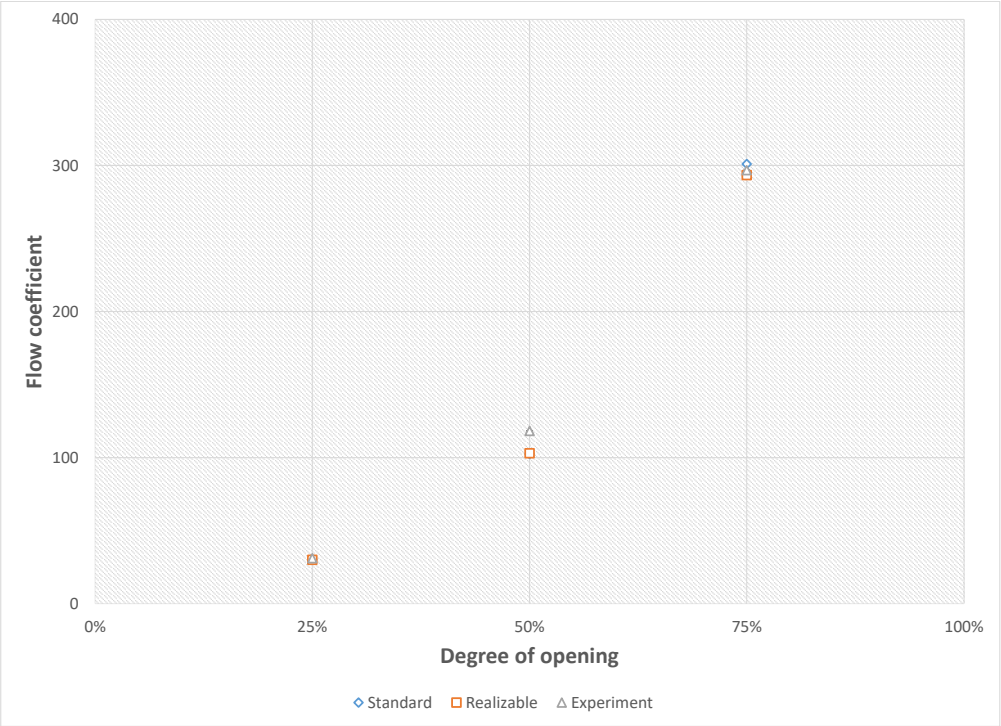

Figure 3.16: Flow coefficients comparison between simulations and experiments of the gate valve

the experimental data, it is probably due to the geometry of the gate valve is more accurately reproduced in the simulations. The flow coefficient prediction for the gate valve at 50% opening is around 13% lower, and it may be a consequence of using a computational mesh with some chamfers removed. The similar explanation applies to the prototypes case, where the rounded edges have been modeled as sharp edges. Additionally, the assembling of the prototype with flange may also account for the higher difference between the experiment and simulations.

Chapter 4

Particle tracking and erosion prediction

In this chapter, sand particles were injected in the continuous phase solved in Chapter 3, and the erosion of the prototypes was estimated following the methodology described earlier. The forces that affect the motion of particles, which are introduced in Chapter 2 were investigated for understanding their effects on particle tracking as well erosion predictions. The influence of restitution coefficients correlations on estimates was assessed. Finally, the three erosion models illustrated in Chapter 2 were applied to estimate the removal of the target material from the particles impingement patterns. The erosion predictions were firstly carried out employing a utility embedded in the Ansys Fluent code; afterwards, an in–house code specifically developed by the FluidLab research group for application to complex geometries was used.

4.1 Particle tracking

The properties of sand particles used in this study are reported in Table 4.1:

Table 4.1: Sand particles properties

$\rho_d(\mathrm{kg/m^3})$	2650
$d_p(\mu\mathrm{m})$	350
$m_p(\mathrm{kg/s})$	0.322
Volume fraction	0.46%

The low volume fraction of sand particles allowed the assumption of one–way coupling. The particle tracking was performed by means of the Discrete Phase Model in

Ansys Fluent code. The model requires firstly to define the forces acting on the particles, which are drag force, gravity and buoyancy, virtual mass force, pressure gradient force and lift force. Drag force is included by default, while other forces are needed to be activated or deactivated by the user. When gravity is activated, the acceleration value of -9.81 m/s^2 along the vertical direction was fed. The virtual mass factor was kept default at 0.5. An user defined function was loaded in body force to replace the Saffman's lift force. Regarding the drag coefficient specification, spherical drag law was considered initially, and the non–spherical factor is equivalent to the shape factor with ϕ being set at 1.0 in Haider and Levenspiel equation (see Equation (2.7)). Then non spherical drag law was applied with non–spherical factor (ϕ) being 0.66, 0.76 and 0.86, which represents the shape of sharp, semi–round and round particles, and the corresponding values of shape coefficients in the E/CRC model (Equation (2.27)) are reported in Table 4.2. Finally, the influence exerted by the turbulence of the fluid on the particle movement was described using Discrete random walk model in Fluent, whose settings were kept default.

Table 4.2: Non–spherical factor and shape coefficient

Non–spherical factor(ϕ)	0.66	0.76	0.86
Shape coefficient(F_s)	1.0	0.53	0.2

The boundary conditions for the parcels are specified as follows. The inlet section was regarded as an injection of particles. For each particle, the position, the velocity, the size as well as other parameters irrelevant to the used model are specified in injection files. The restitution coefficients in boundary conditions of walls are set as units or polynomial functions according to Forder or Tabakoff correlations (Equation 2.18 and 2.19). And in the pressure–outlet, the discrete phase boundary condition type was "escape".

The tracking of the particle trajectories stops either when a particle leaves the domain or when a maximum number of time steps is reached. During tracking, it was found that the proper maximum number of steps was around 40000, 25000 and 20000 for 25% opened, 50% opened and 75% opened domains accordingly to guarantee that the number of incomplete particles accounting for less 0.5% of the injection.

4.2 Preliminary erosion predictions using the utility embedded in Ansys Fluent

The Ansys Fluent code is equipped with an utility for erosion estimation, which requires the user to define an erosion model. This can be done in two ways, namely by the User–Defined Function or by a polynomial formula. The latter is a particular case of the general formula (Equation 2.20) covered in Chapter 2, in which K is a polynomial function of the particle size, here too as a constant calculated on the actual value of d_p, and $f(\alpha)$ is a polynomial function of the impact angle α. The erosion models (Equation 2.21, 2.23 and 2.27) were all rearranged to this form. This was done accounting for the characteristics of the simulated test case, the properties of sand particles have been concluded (Table 4.1), other conditions are presented in Table 4.3. In order to express the particle impact function as a polynomial formula: $f(\alpha) = \sum_{i=0}^{5} A_i \alpha^i$, the interpolation for DNV–GL and Oka et al. models is needed. Table 4.4 and Table 4.5 summarize the parameters of the erosion models:

Table 4.3: Physical conditions tested in Fluent

Type of geometry	50% opened prototype
Material of walls	Aluminum
Hv(Aluminum)	1.12 GPa
ρ_t(Aluminum)	2700 kg/m^3
F_s(Sand)	0.2(round shape)
Flow velocity	5 m/s

Table 4.4: Values of constants and velocity exponents

	K	n
DNV–GL	5.8×10^{-9}	2.3
E/CRC	2.96×10^{-9}	2.41
Oka et al.	3.74×10^{-9}	2.31

An analysis of the consistency of the wear estimates with respect to purely numerical settings was performed. Like the flow coefficient, they are influenced by the quality of the mesh. Furthermore, the number of injected parcels also has effect on the erosion prediction, and, essentially, the more parcels for a constant mass flow rate of

Table 4.5: Values of constants and velocity exponents

	DNV–GL	E/CRC	Oka et al.
A_0	0	0	5.48×10^{-3}
A_1	7.47×10^{-2}	9.43×10^{-2}	1.67×10^{-1}
A_2	-1.77×10^{-3}	-3.08×10^{-3}	-6.41×10^{-3}
A_3	1.51×10^{-5}	5.81×10^{-5}	1.13×10^{-4}
A_4	-4.17×10^{-8}	-5.87×10^{-7}	-9.80×10^{-7}
A_5	0	2.30×10^{-9}	3.40×10^{-9}

particles contains, the more precise the solution is expected to be. Thus, wear should be independent to the number of cells as well as the number of injected parcels.

And Figure 4.1 shows the sensitivity of erosion for the prototype at 50% opening. The other settings of the computational model which can potentially affect the wear predictions were kept constant. Particularly, only the drag force was activated; restitution coefficients were set to units; particles followed spherical law; and DNV–GL erosion model was used.

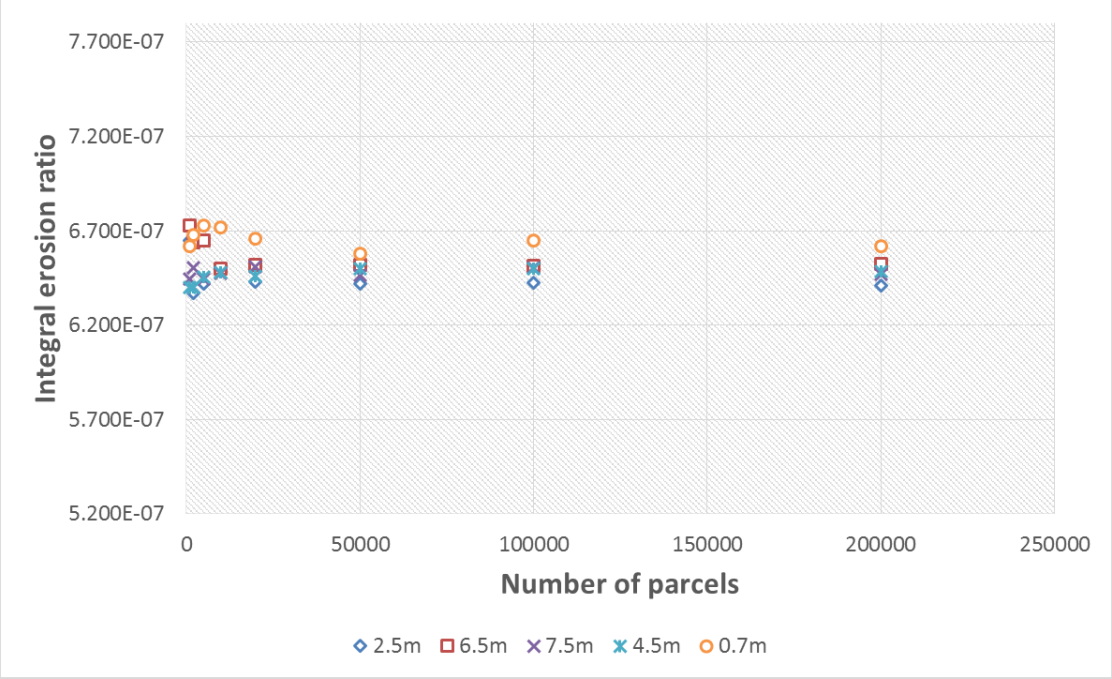

Figure 4.1: Ansys Fluent predictions: integral erosion ratio on all the walls of the domain versus number of parcels for different computational meshes.

In Figure 4.1, "0.7m", "2.5m"... refers to the computational domain with "0.7", "2.5"... million cells. It is found that when the number of parcels is 50000 or higher,

the integral erosion ratio is considered independent to the number of parcels. And it is also noticed, when the number of grids reaches 4.5 million or higher, the variation of the integral erosion ratio becomes very small. In conclusion, it is considered that the integral erosion ratio is essentially independent upon the number of parcels and number of cells at 50000 and 4.5 million respectively.

This preliminary study and few other simulations led to the decision of using an in–house code developed by the FluidLab research group for erosion prediction instead of the Ansys Fluent module. The motivation is explained as follows:

1. The in–house code allows the possibility of better controlling the erosion calculation procedure;

2. It is specifically made for handling complex geometries with components characterized by different materials, while it is rather difficult doing the same thing in Ansys Fluent;

3. It is capable of defining more precise erosion model using analytical impact angle functions directly. The User–Defined Functions can achieve the same goal but require great efforts, while the polynomial approximation may lead to discretization errors.

4.3 Erosion prediction using the FluidLab in–house code

The main features of the in–house code for erosion estimation developed by the FluidLab group are displayed as Figure 4.2. In the blocks, the term, "nearestcentroids" refers to the vectors that contain the fluid–dynamic characteristics of the parcels at the stage of their impingement against the wall boundaries.

As already mentioned, one of the main advantages of the in–house code is that it can easily allow for the definition of different wall assemblies characterized by different materials. Here, the "valve region", previously introduced in Chapter 3, was divided into two parts: Proto (surface mesh of the obstacle) and Fake valve body (surface mesh of the rest of valve region). Figure 4.3 shows the boundary meshes of these two components.

Consistent with the characteristics of the experiments which will be performed in the Hydraulic Laboratory, the wall material of the Proto was aluminum, while wall

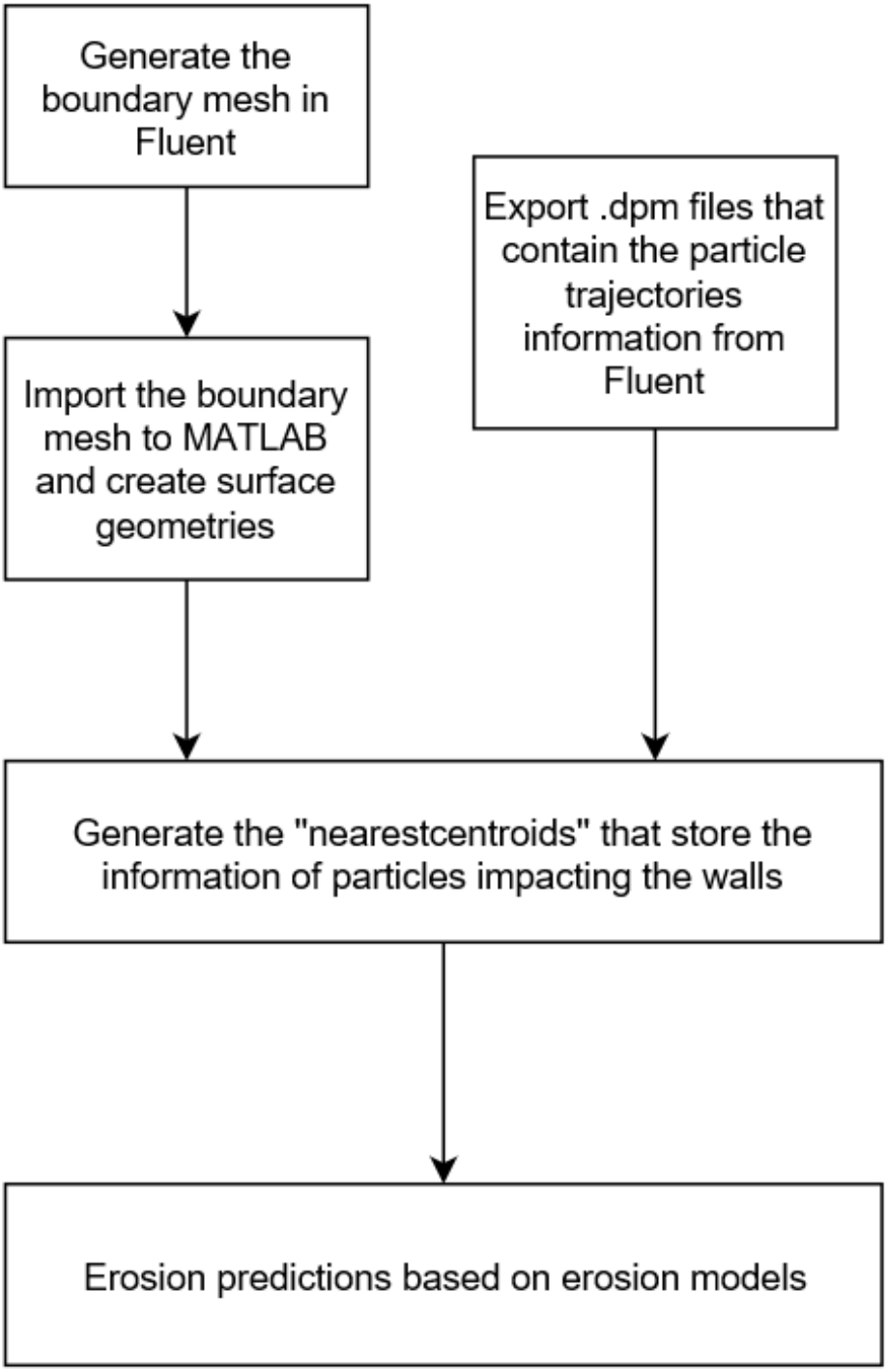

Figure 4.2: Main blocks of the erosion prediction code developed by the FluidLab research group

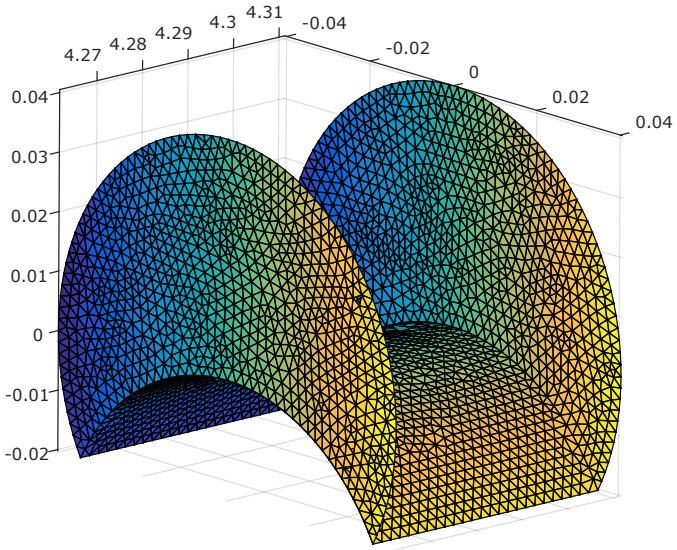

(a) Proto

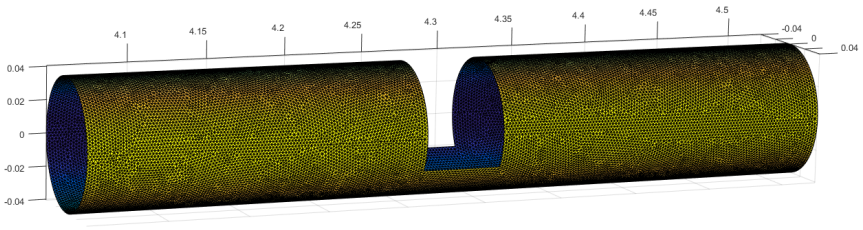

(b) Fake valve body

Figure 4.3: The Proto and Fake valve body

material of the Fake valve body was AISI304, the densities and Vickers numbers are reported in Table 4.6.

Table 4.6: Properties of Aluminum and AISI304

	Aluminum	AISI304
Density(kg/m^3)	2700	8000
Vickers number(GPa)	1.12	1.29

The in–house code allowed for the evaluation of the integral erosion ratio of Proto, Fake valve body, and their sum, which is referred to as total integral erosion ratio (total IER).

4.3.1 Consistency analysis

The consistency analysis with respect to the number of injected parcels and the number of computational cells was repeated with the in–house code. The mesh with 4.5 million cells was chosen for sensitivity study on number of parcels. Other settings were: all forces were considered with virtual mass factor equaling to 0.5; non spherical factor was set to 0.76 accounting for the shape of particles; Forder et al. correlations were used for restitution coefficients; Oka et al. erosion model was selected. The result is reported in Table 4.7 and Figure 4.4.

Table 4.7: Total IER with respect to number of parcels

Number of parcels	Total IER
1000	1.19×10^{-6}
10000	1.24×10^{-6}
20000	1.27×10^{-6}
50000	1.29×10^{-6}
100000	1.28×10^{-6}

As the number of parcels reaches 20000 or higher, the integral erosion ratio is practically constant. Therefore, it is concluded that the injection with 50000 parcels is sufficient for attaining consistent erosion predictions, as also suggested in previous section. Another sensitivity analysis is about the number of computational cells, with fixed injection of 50000 parcels. The result is found in Table 4.8 and Figure 4.5.

The total integral erosion ratio is not very sensitive to the mesh with 4.5 million cells or higher. Thus, the 4.5 million cells mesh was used from this point onwards.

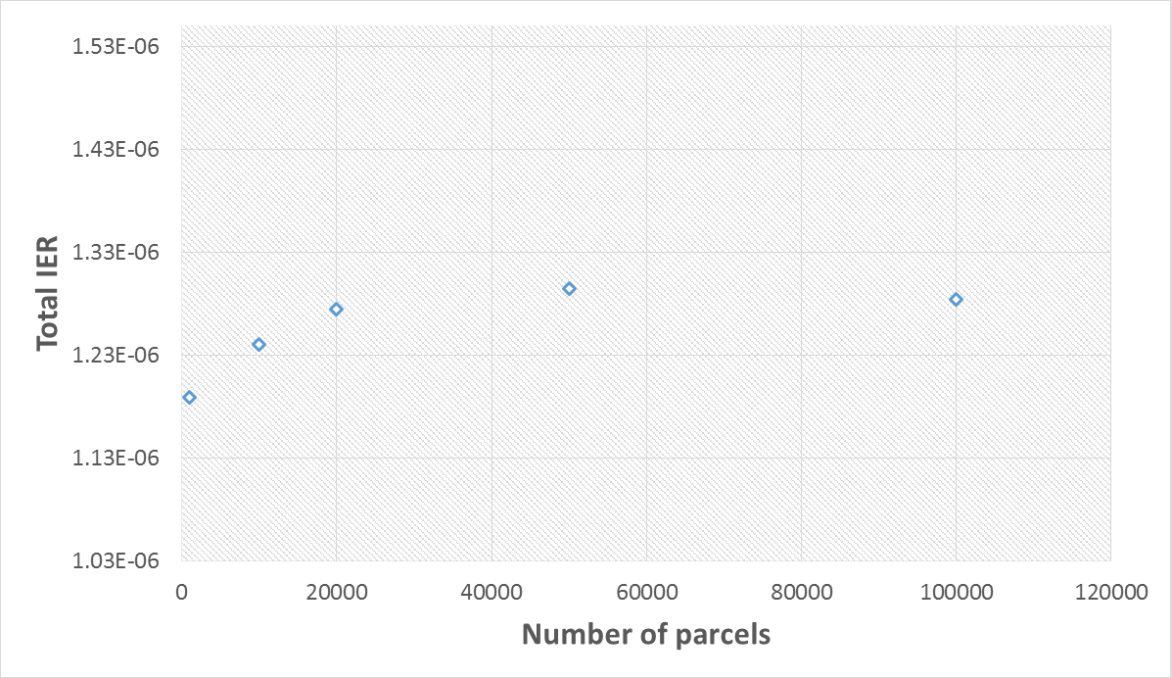

Figure 4.4: Sensitivity of total IER to number of parcels (50% opening)

Table 4.8: Total IER with respect to number of computational cells

Number of computational cells	Total IER
0.7×10^6	6.36×10^{-7}
1.3×10^6	7.67×10^{-7}
4.5×10^6	1.29×10^{-6}
6.5×10^6	1.24×10^{-6}
7.5×10^6	1.35×10^{-6}

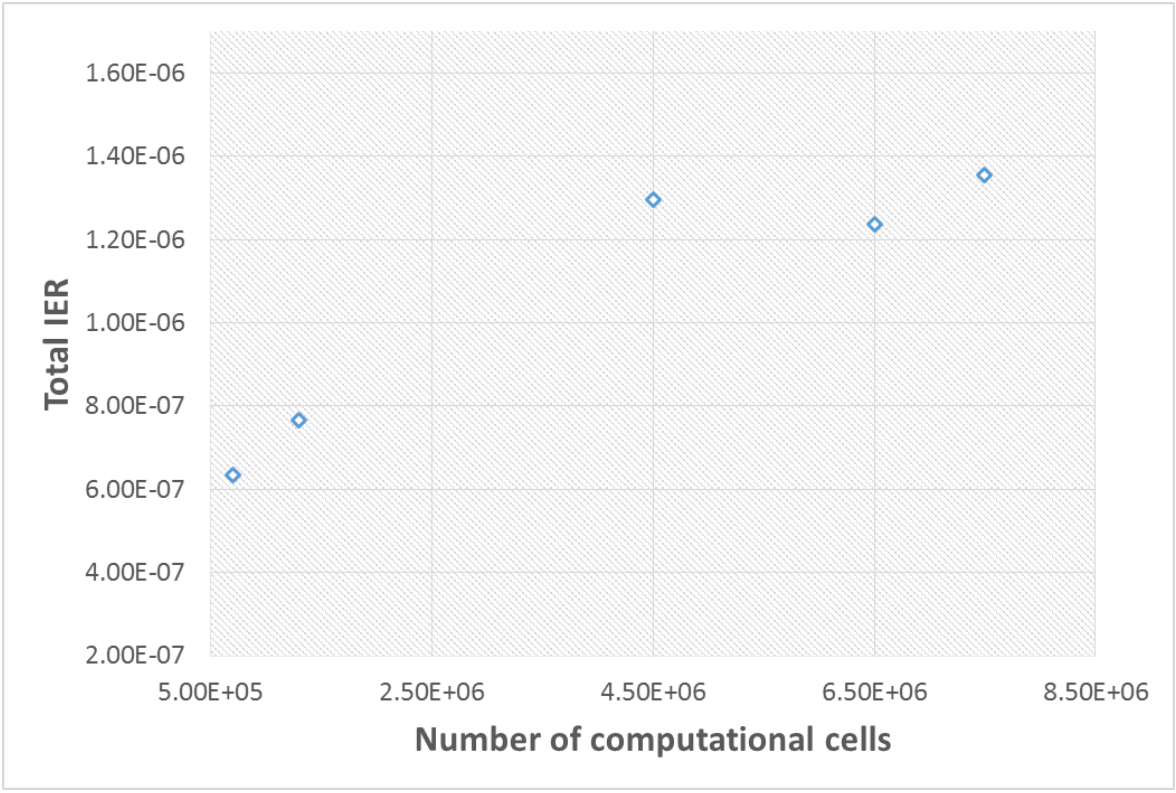

Figure 4.5: Total IER sensitivity to number of computational cells

The locations of erosion are shown in Figure 4.6. The most eroded surfaces are the upstream corner of the Proto as well as the part of Fake valve body under the Proto. The severity of erosion on Fake valve body is high, requiring further studies. Hence, the three cross sections that normal to the axis of the pipe were created, and they are, in fact, arcs because they are on the surface of Fake valve body. Marked as UP, MID and DOWN, these sections are located in the front of, in the middle of and behind the Proto (see Figure 4.6b). The penetration depth along these arcs varies and is a function of angle θ, which is defined as the deviation from vertical direction, as shown in Figure 4.7.

Figure 4.8 shows the effect of the number of parcels in injection on the penetration rate profiles on the UP, MID, and DOWN sections. The highest penetration rate was observed in MID section, consistent with the observation in Figure 4.6; with the increase of number of parcels, the penetration rate along these arcs changes more smoothly and more physically reasonable, indicating that sufficient number of parcels is necessary for reliable wear estimates.

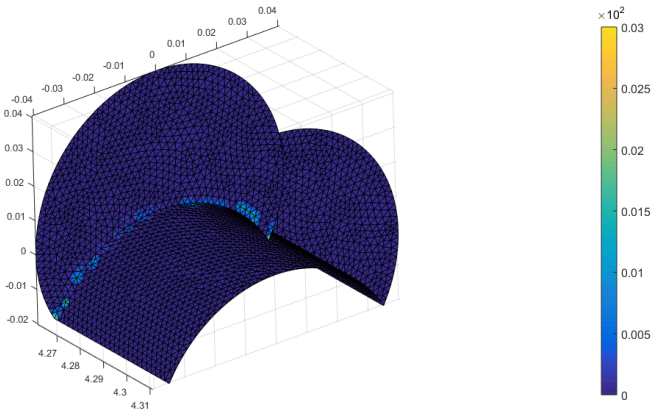

(a) Erosion location in Proto

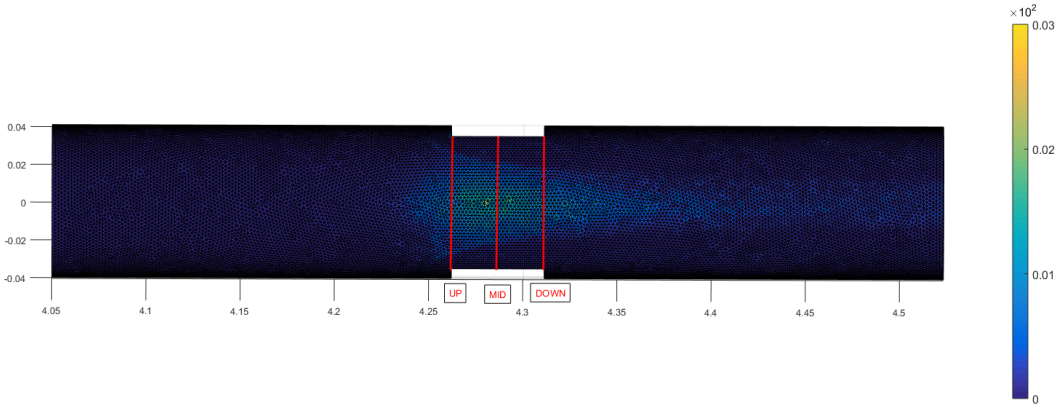

(b) Erosion location on Fake valve body

Figure 4.6: Erosion locations in the valve region

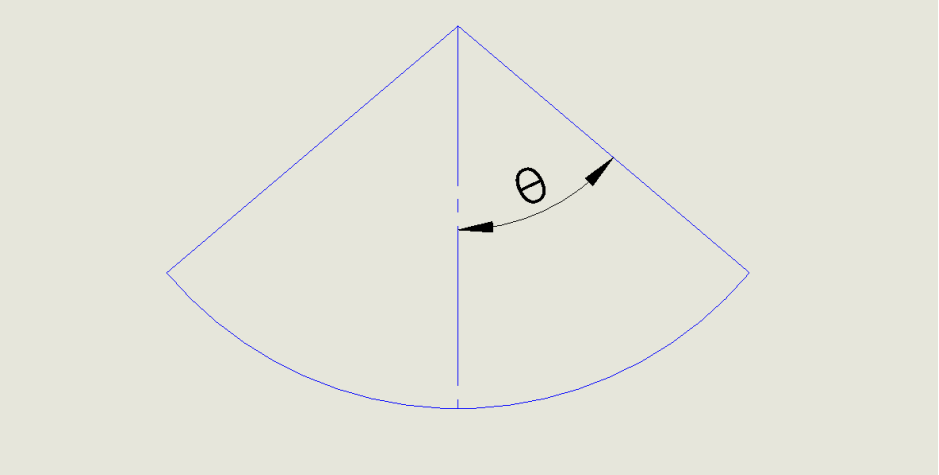

Figure 4.7: Explaining the deviation angle θ for sections UP, MID and DOWN

4.3.2 The effects of sub–models and parameters of the erosion prediction model

It is well known that the computational model for erosion predictions consists of many sub–models and parameters which can affect the wear estimates. Messa and Malavasi[15] quantified the effect of each of them on the benchmark case of abrasive jet impingement test. In this section, a similar analysis was performed for the 50% prototype, based on the mesh with 4.5 million cells and the injection with 50000 parcels, as suggested in the consistency analysis.

These parameters are the forces included in the equation for particle motion (lift force, pressure gradient force, virtual mass force, gravity and buoyancy), the two non–spherical factors (0.66 and 0.86), unit and Grant & Tabakoff restitution coefficients correlations, and E/CRC and DNV–GL erosion models other than Oka et al. erosion model.

By changing only one parameter each time, the influence that these parameters on integral erosion ratio are summarized in Table 4.9. Influences from forces should not be neglected according to this study, the minimal effect comes from virtual mass force, but still, not including it can cause 13% variation in prediction. Regarding the non–spherical factor, the more rounded particles may be less affected by drag force, therefore probably have better chance traveling through the boundary layer and impacting the wall, causing more material loss, thus the integral erosion ratio would be higher for particles with higher non spherical factor. Among the restitution coefficients correlations, highest integral erosion ratio was observed by using Grant & Tabakoff correlations, while using unit restitution coefficients led to the lowest prediction, but

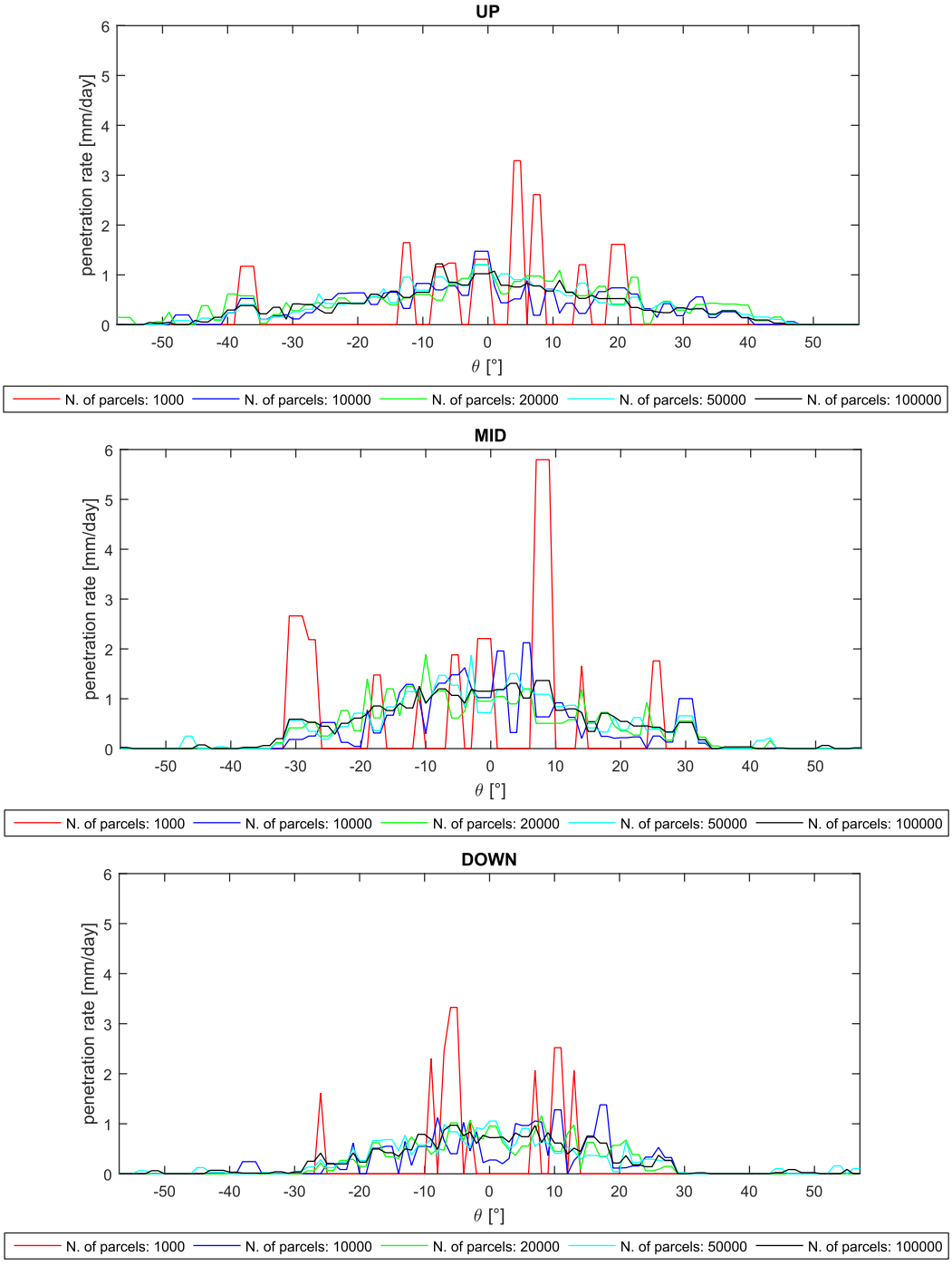

Figure 4.8: Penetration rate on sections UP, MID and DOWN for different number of parcels

Table 4.9: Effects of various parameters on integral erosion ratio

Conditions in simulation	Total IER
Reference	1.29×10^{-6}
Without Lift Force	6.58×10^{-7}
Without Pressure Gradient Force	1.52×10^{-6}
Without Virtual Mass force	1.46×10^{-6}
Without Gravity	1.04×10^{-6}
$\phi = 0.66$	9.80×10^{-7}
$\phi = 0.86$	2.10×10^{-6}
Unit Restitution coefficients	1.14×10^{-6}
Grant & Tabakoff correlation	1.55×10^{-6}
E/CRC model	4.25×10^{-7}
DNV–GL model	2.23×10^{-7}

the differences are not significant compared to other parameters. Finally, Oka et al. erosion model produces the highest erosion prediction. And the prediction by DNV–GL model is one order of magnitude lower.

Similarly, the penetration rate graphs concerning the influences from these parameters are presented. Figure 4.9 shows that gravity has great effect on the distribution of eroded surfaces, and a comparison of erosion locations on Fake valve body with or without gravity is shown in Figure 4.10; much lower penetration rate for the case without the lift force included; the virtual mass force and pressure gradient force proved to have less effects compared to other forces. However, when changing the shape of particles (by changing the non spherical factor), the variation of penetration rate is significant, as observed from Figure 4.11. Figure 4.12 shows that the effect on penetration rate by changing restitution coefficients correlations is actually not huge in this study. The effects of erosion models on penetration rate are displayed in Figure 4.13, and it is concluded that the Oka et al. model makes much higher erosion predictions than other two models.

4.3.3 Erosion predictions of prototypes at other openings

The erosion predictions have been also carried out for the two other prototypes (see Figure 3.4). In order to preliminary assess the effect of valve opening on wear characteristics. The consistency of the estimates with respect to the number of parcels might

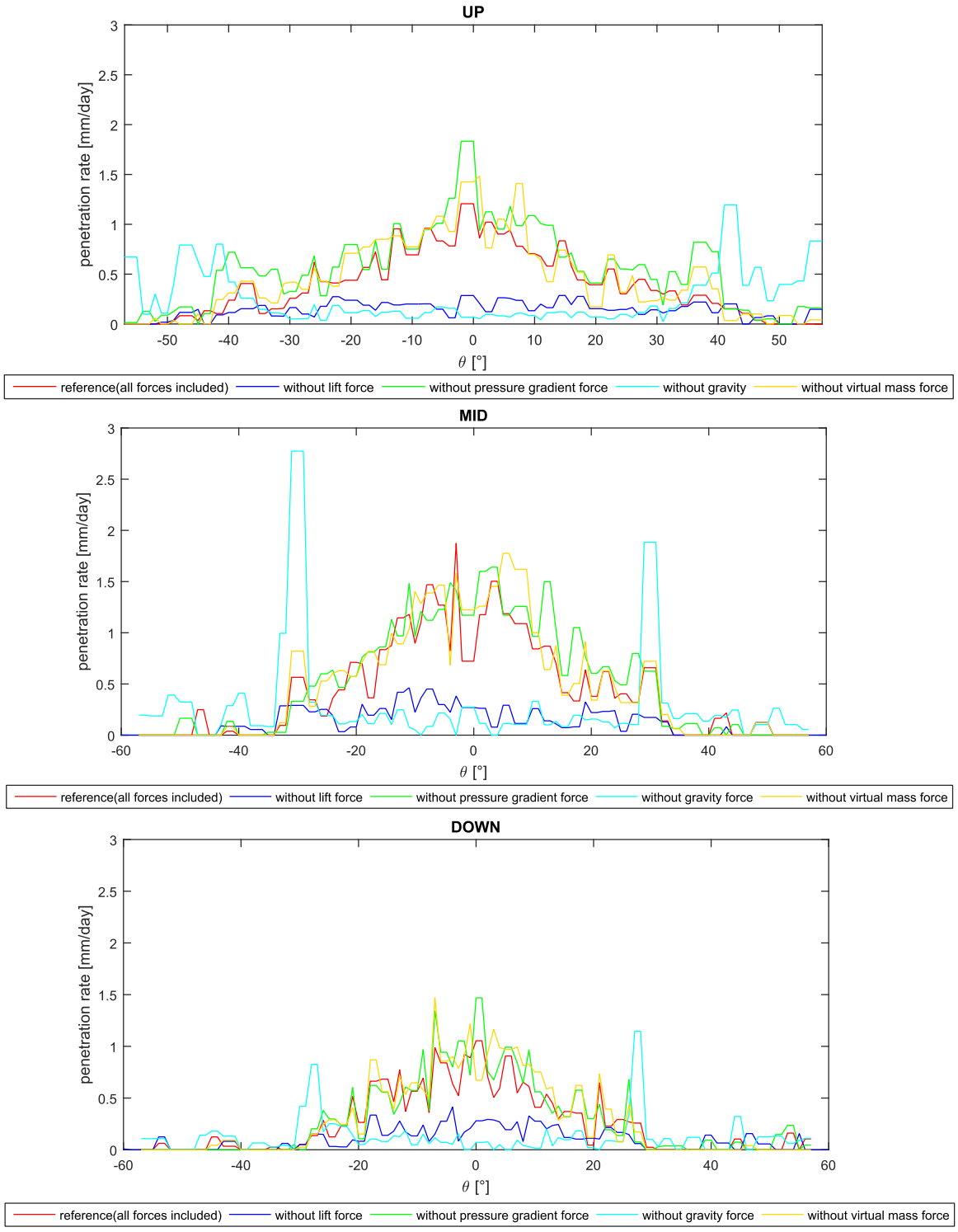

Figure 4.9: Effects of forces on penetration rate (50%)

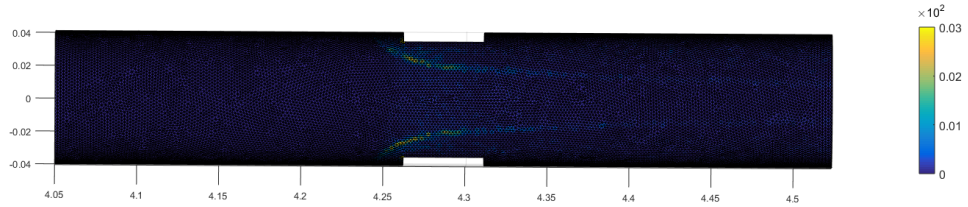

(a) Erosion locations without gravity included

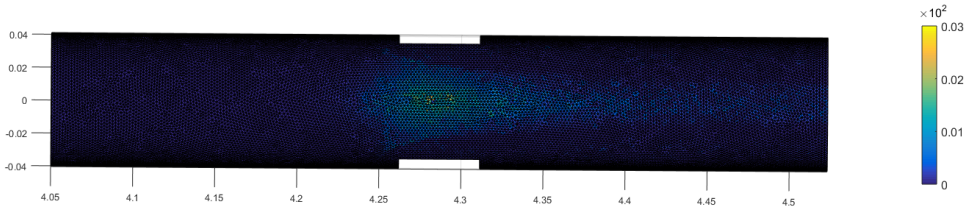

(b) Erosion locations with gravity included

Figure 4.10: Effects of gravity on erosion location distribution

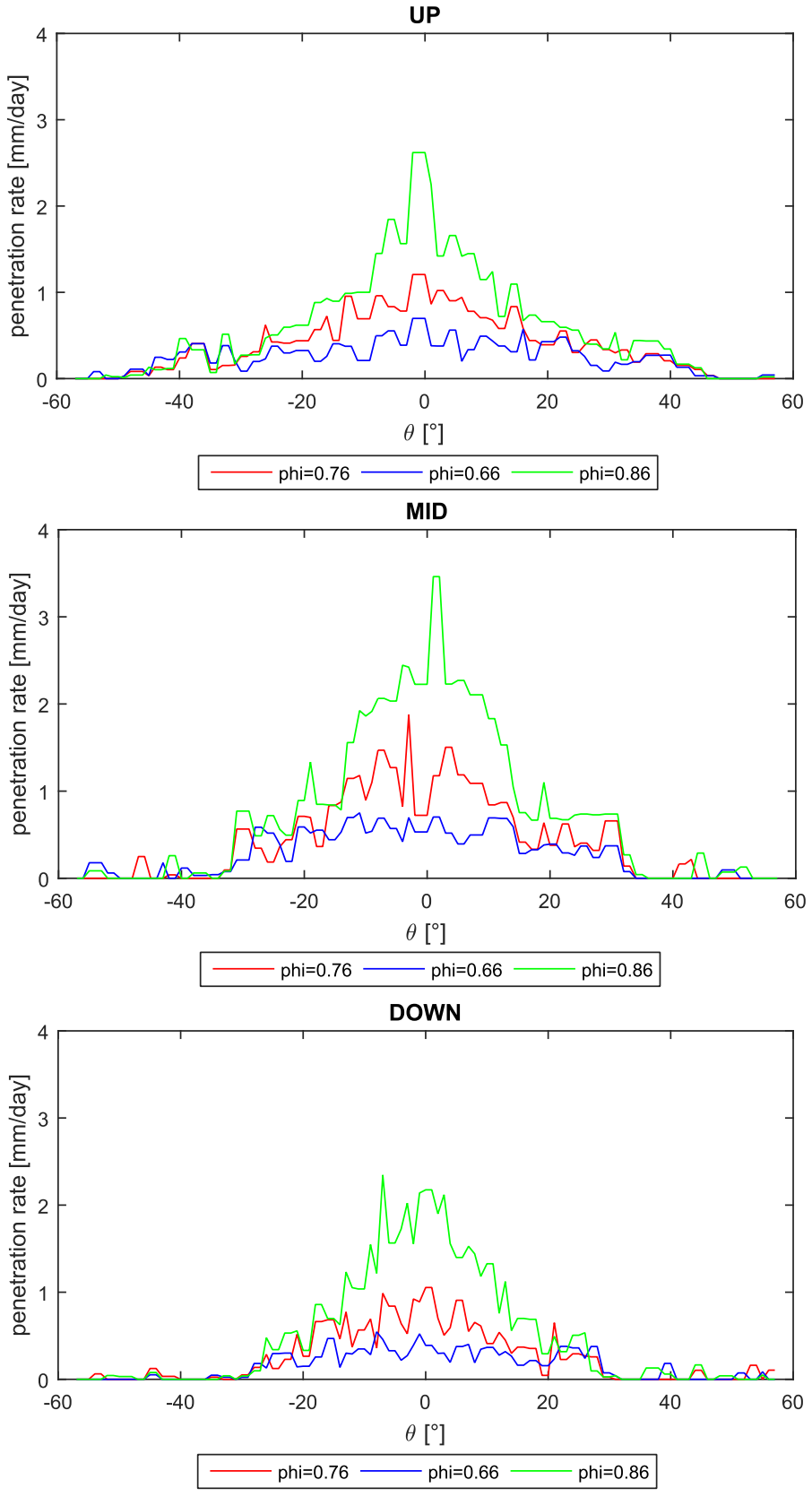

Figure 4.11: Effects of non–spherical factors on penetration rate (50%)

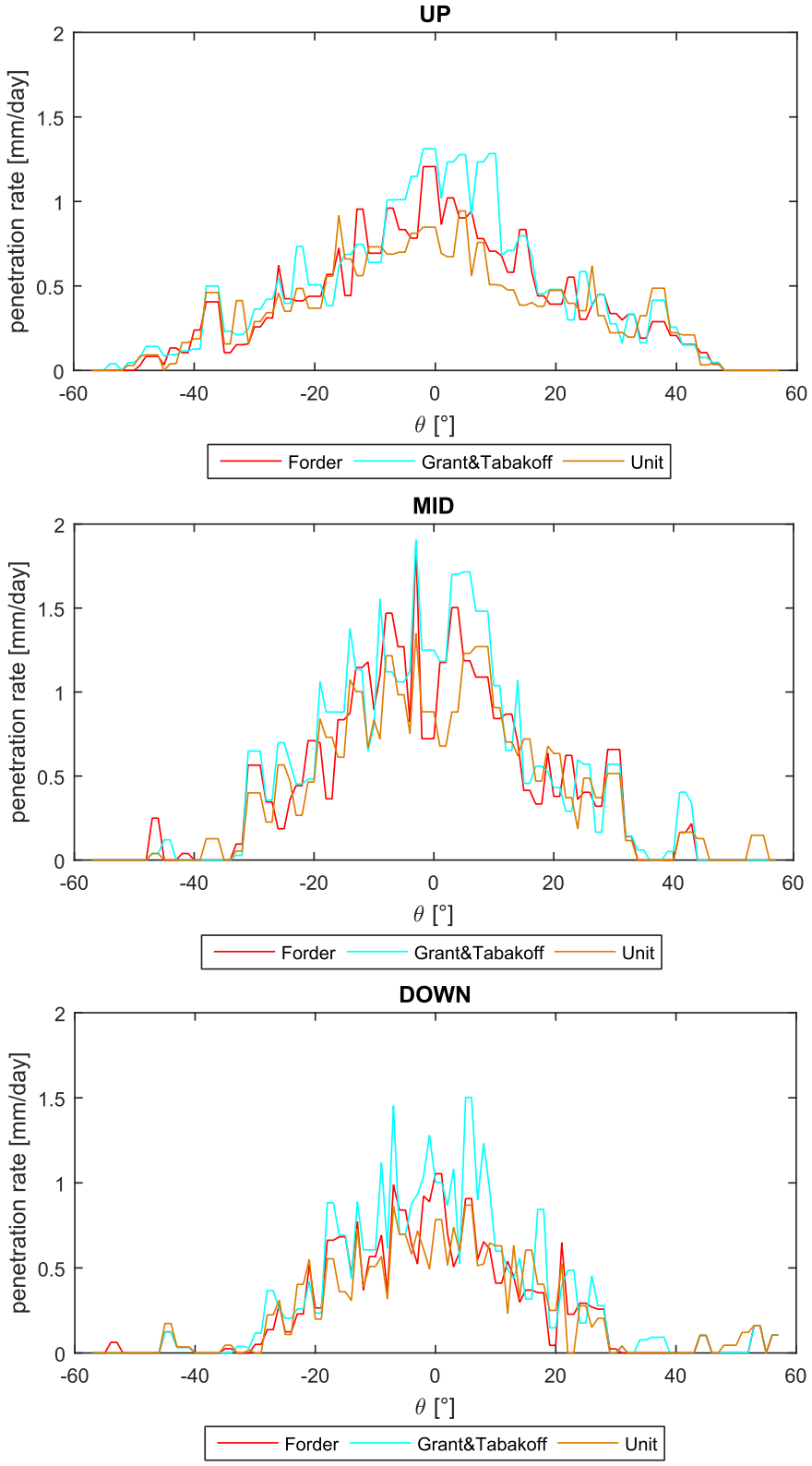

Figure 4.12: Effects of restitution coefficients on penetration rate (50%)

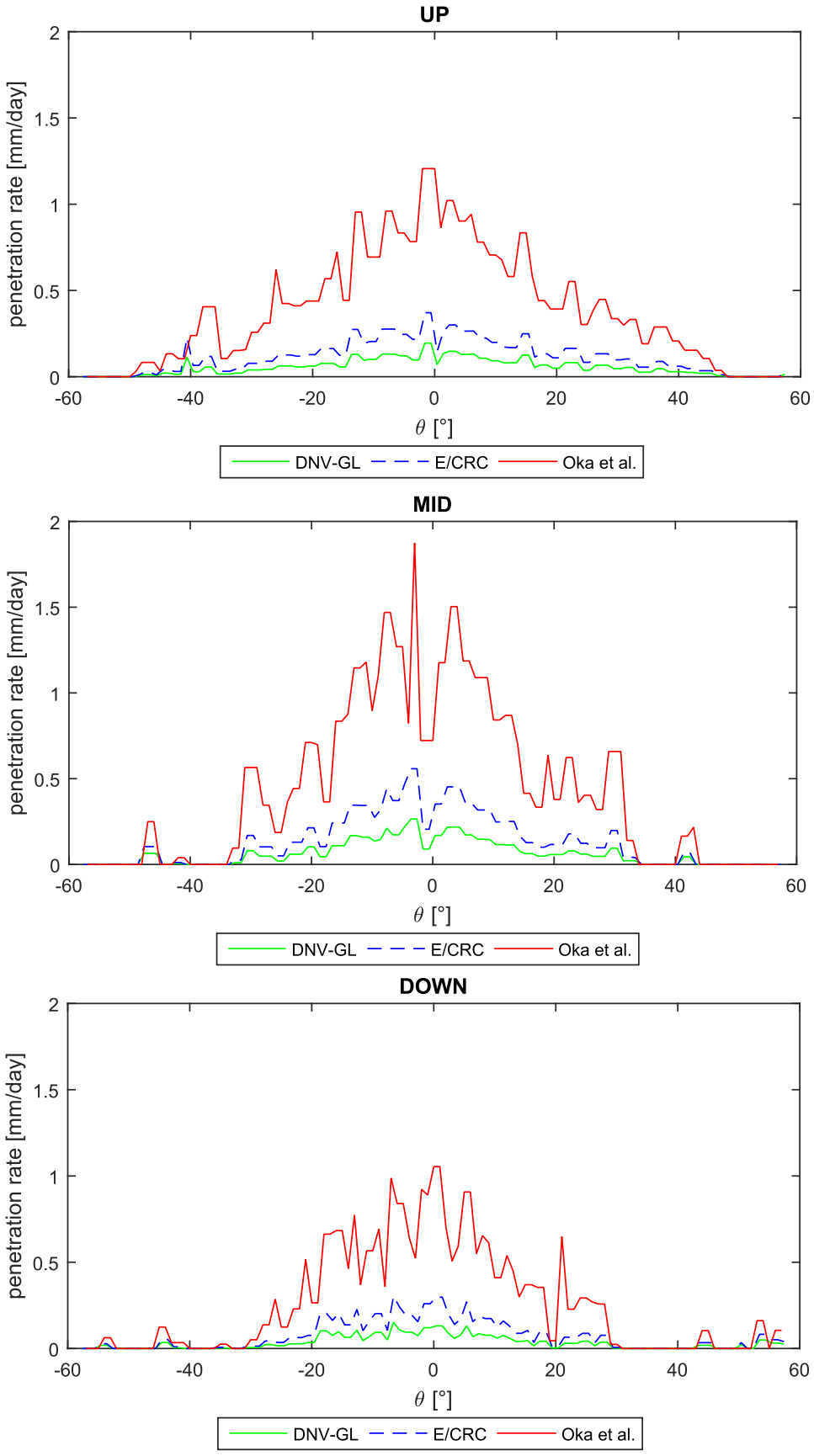

Figure 4.13: Effects of different erosion models on penetration rate prediction (50%)

change if the prototype at a different opening was used. But, as indicated in Table 4.10, the injection with 50000 parcels is appropriate for prototypes at 25% opening and 75% opening as well. In these simulations, the settings of computational model were the same as for the consistency analysis of the 50% prototype. The computational mesh consists of 5.0 million cells for 25% opening and 5.1 million cells for 75% opening.

Table 4.10: Total IER with respect to number of parcels(25% and 75% openings)

Number of parcels	25% opening	75% opening
20000	7.56×10^{-5}	4.03×10^{-7}
50000	7.64×10^{-5}	3.93×10^{-7}
200000	7.64×10^{-5}	3.95×10^{-7}

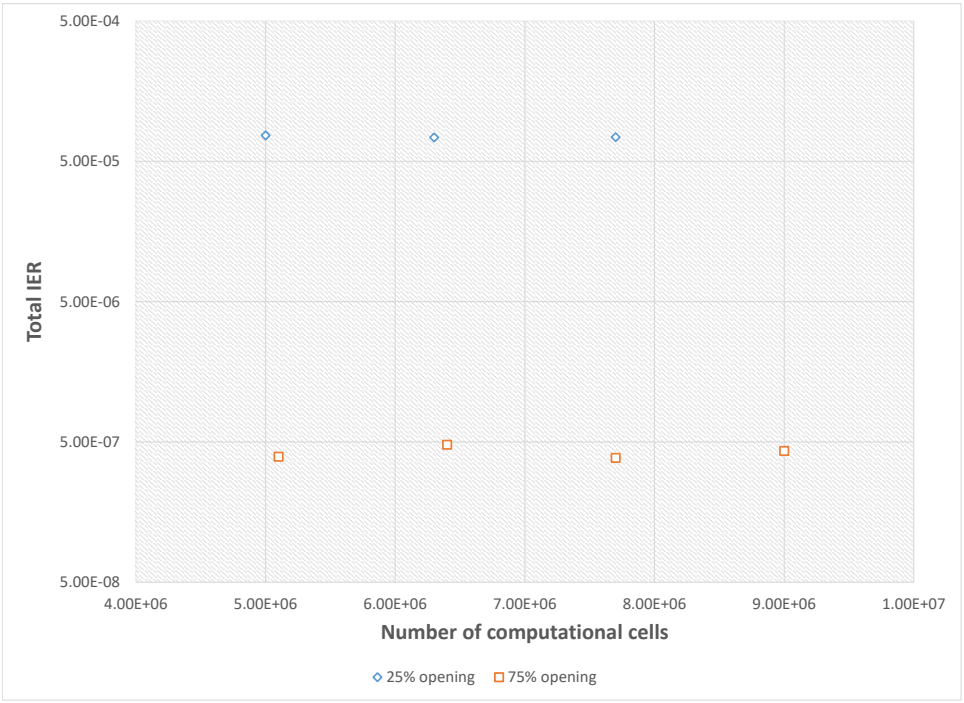

Figure 4.14: Grid independence of erosion in the prototypes at 25% and 75% openings

The sensitivity analysis subjects to the number of cells in the domain was also carried out for these two openings. Note that in the previous single–phase simulation, there is some convergence issue regarding to the domain of 25% opened prototype with 9.0 million cells, hence, this mesh has been discarded in this analysis. Figure 4.14

illustrates the grid independence study of integral erosion ratio. The integral erosion ratio of 75% opened prototype is rather sensitive to the mesh, and this is probably due to the erosion ratio being too small, and the prediction is easily affected. In fact, this parameter is one magnitude lower than the IER of 50% opened prototype and two magnitudes lower than the IER of 75% opened prototype, revealing that the wear estimates are significantly affected by the degree of openings of valves. The comparison of penetration rate, as shown in Figure 4.15, also illustrates this difference.

And the non–spherical effects are presented by Figure 4.16 and Figure 4.17. The erosion locations would not be deeply affected by the shape of particles, but the penetration rate experiences a significant increase when the non–spherical factor is higher, indicating that the in this particular case, the round particles would cause more severe erosion.

4.3.4 Improvements in the modeling of the actual rig test section

In the test rig, the obstacle and the pipe were assembled together by fixing the flange to the pipe (see Figure 3.1). Because the flange is made of aluminum instead of AISI304 in pipe, the erosion behavior might change, though the the flange is only 11 mm long. Additionally, there is also a part of pipe measured 1430 mm long downstream of the prototype (Figure 4.18), which should also be included in the simulation. With the purpose of better characterizing the erosion phenomena in the test rig experiments, new boundary meshes were created, as shown in Figure 4.19.

However, unexpected results led to the decision of investigating the sensitivity of the wear estimates on the surface mesh that are used to define the wall boundaries. The analysis reveals the effect being not always negligible, which definitely deserves more attention. For the moment, the comparison was made on the new surface mesh to attain consistent results. The earlier case was re–enabled by assuming the flange to be made of AISI304.

Table 4.11 reports the difference of integral erosion ratio of the “Flange” made of Aluminum or AISI304. It is conclude that, when considering the flange with the right material, the erosion of this region will decrease in this region, but the overall erosion of the valve region, which is referred to the combination of “Proto”, “Fake valve body”, and “Flange” is not substantially affected. An attempt to interpret this behavior is made as follows. In Oka et al. erosion model, the integral erosion rate is proportional to the target material density, the mass flow rate of sand particles is constant, thus the

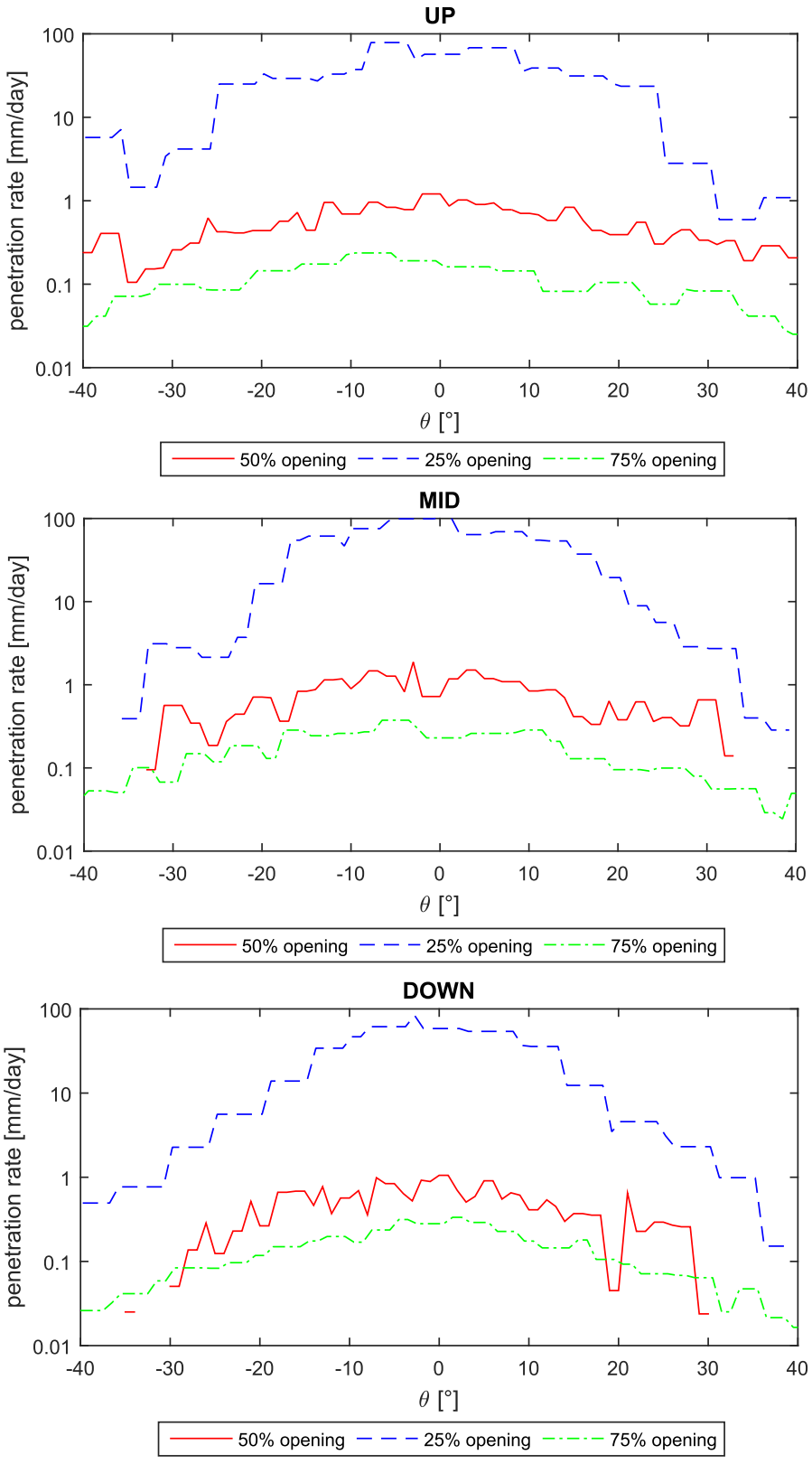

Figure 4.15: Effects of degree of opening on penetration rate

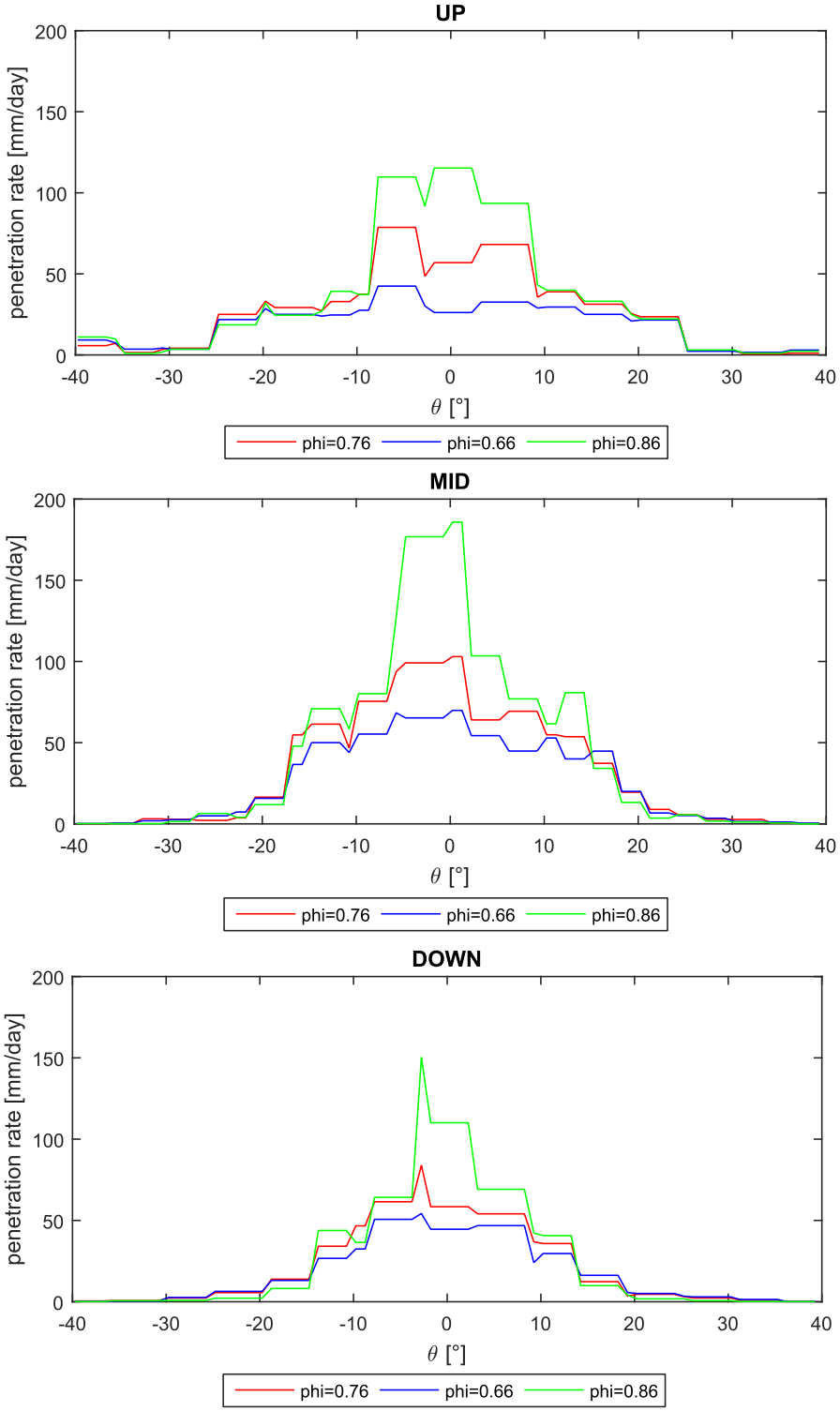

Figure 4.16: Effects of non–spherical factors on penetration rate (25%)

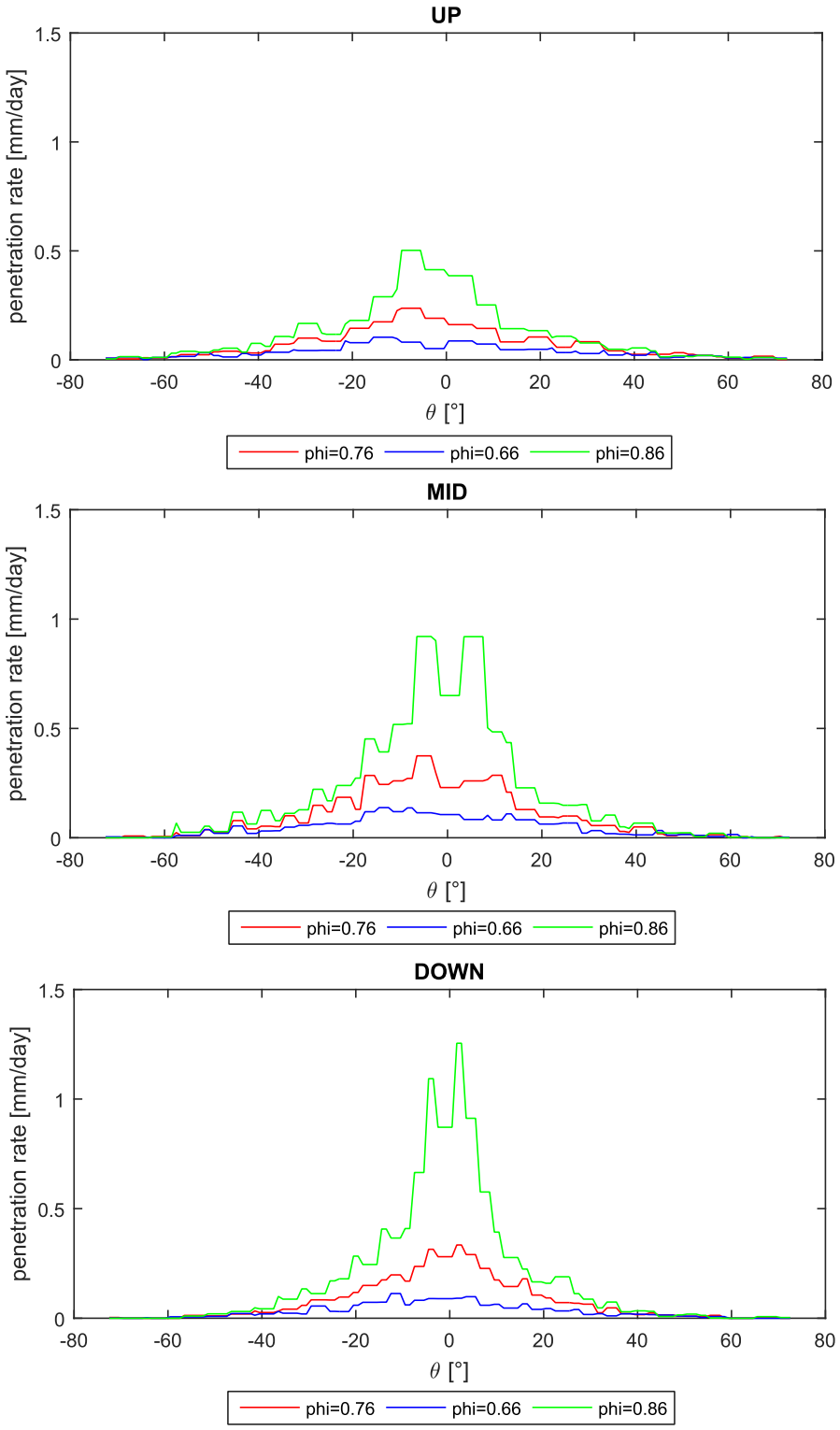

Figure 4.17: Effects of non–spherical factors on penetration rate (75%)

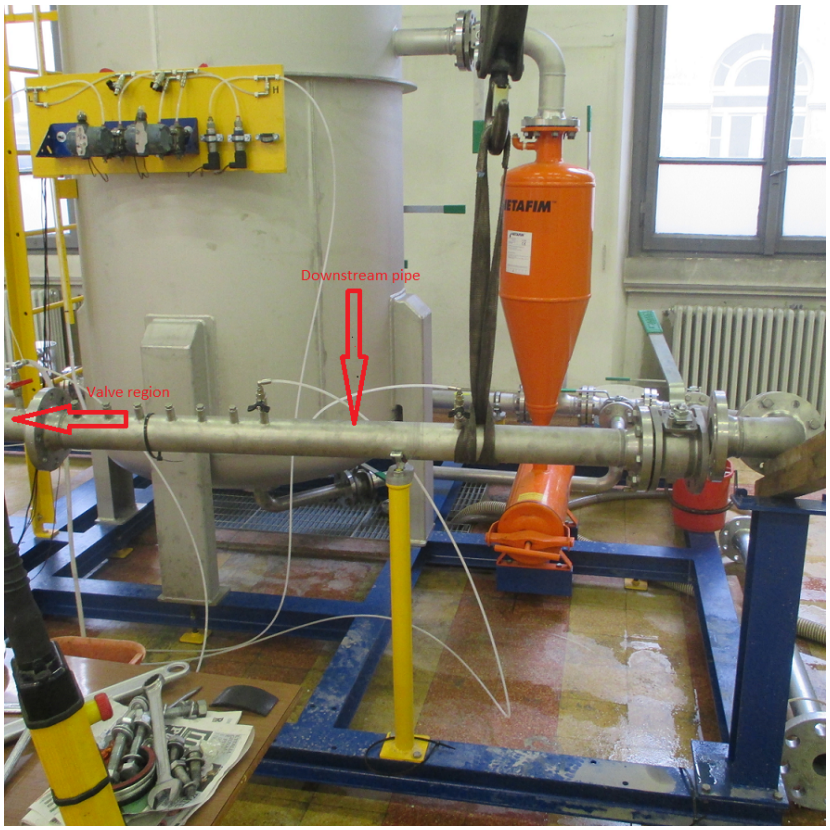

Figure 4.18: Photo of the test rig

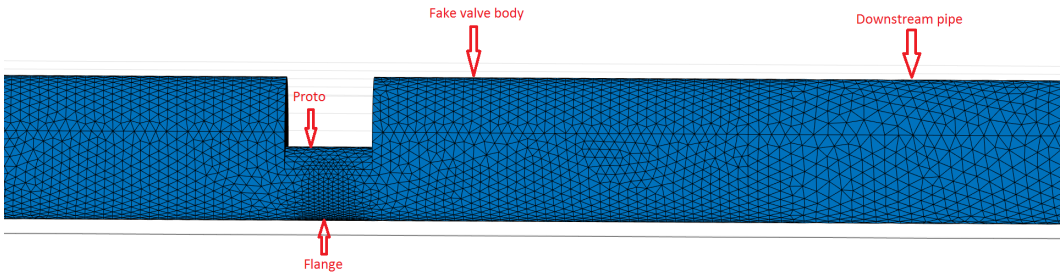

Figure 4.19: New boundary mesh that contains flange

Table 4.11: Effect on IER while adding the flange

Openings	Flange material	IER(Flange)	Total IER
25%	Aluminum	2.06×10^{-6}	7.23×10^{-5}
	AISI304	5.61×10^{-6}	7.58×10^{-5}
50%	Aluminum	4.91×10^{-8}	1.69×10^{-6}
	AISI304	1.33×10^{-7}	1.77×10^{-6}
75%	Aluminum	1.01×10^{-8}	3.99×10^{-7}
	AISI304	2.72×10^{-8}	4.16×10^{-7}

integral erosion ratio is proportional to the wall density. Hardness is a parameter that decides the difficulty of removing material by sand particles. Notice that the hardness of AISI304 is a little higher than the hardness of Aluminum, meaning that the volume of material loss for AISI304 would be a bit lower than the volume loss for Aluminum (Table 4.12). Combining these two effects, the mass loss for AISI304 is expected higher than for Aluminum.

Table 4.12: Volume losses comparison between two materials

	Aluminum	AISI304
Density (kg/m^3)	2700	8000
Hv (Gpa)	1.12	1.29
Mass loss (kg/s)	4.91×10^{-8}	1.33×10^{-7}
Volume loss (m^3/s)	1.82×10^{-11}	1.66×10^{-11}

The MID section is exactly in the middle of the flange, so the penetration rate of the flange can be expressed by the penetration rate along MID circle. The penetration rate for Aluminum is only slightly higher than the penetration rate for AISI304, as shown in Figure 4.20, indicating that the volume removal of the flange in Aluminum is a little higher.

Table 4.13: IER of both downstream pipe and valve region

Degree of opening	IER(Downstream pipe)	IER(valve region)
25%	2.52×10^{-5}	7.23×10^{-5}
50%	2.90×10^{-6}	1.69×10^{-6}
75%	1.67×10^{-6}	3.99×10^{-7}

Downstream pipe, as an important part in the test rig, was also simulated and

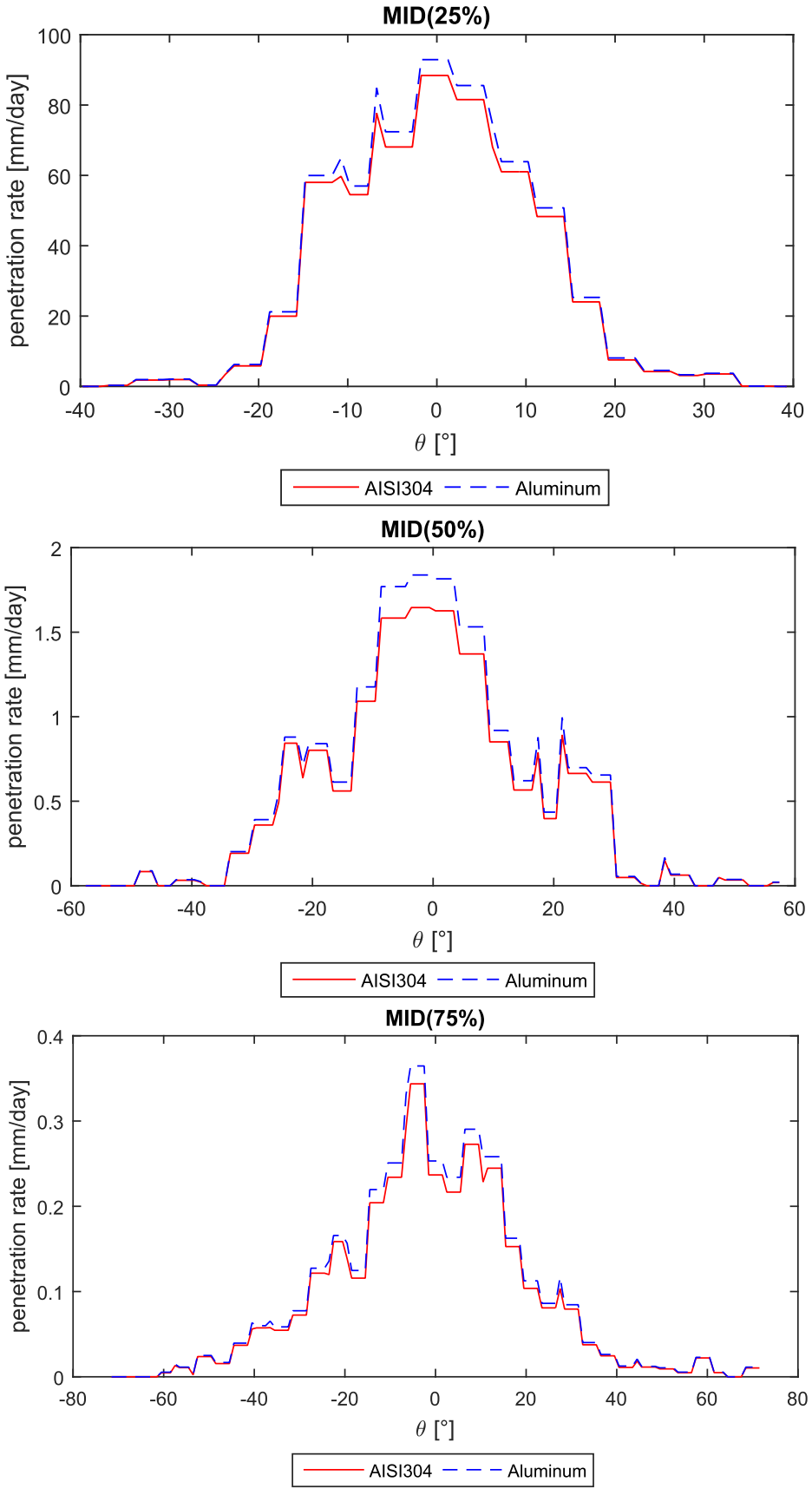

Figure 4.20: Penetration rate of the flange

the erosion data were reported in Table 4.13, together with the integral erosion ratio of the valve region. It is evident that the integral erosion ratio of the downstream pipe is in the same magnitude of the valve region, hence it is not negligible. For the prototypes with 50% opening and 75% opening, the most material losses were found in the downstream pipe. And this is a very important information for the design of the laboratory experiments.

Chapter 5

Conclusion

In this thesis, the impact erosion of a gate valve subjected to the impingement of sand particles in water flow was preliminary studied by CFD, in order to plan a future experimental campaign. Three prototypes of a gate valve at different openings were simulated, as these will be the first tested geometries in the laboratory. Based on the pertinent literature, the investigation was conducted following a procedure consisting of liquid–phase flow modeling, Lagrangian tracking of the particle trajectories, and wear estimation by applying erosion models.

At first, the single–phase flow fields in both prototypes and gate valve were solved under steady state assumption. The main focus of this part was the estimation of the flow coefficient, introduced by the international IEC standard for quantifying the dissipation characteristics of hydraulic devices. Two turbulence models, standard k–ε and realizable k–ε, were supplied as turbulence closures. A series of computational grids ranging from a few million cells to nearly ten million cells were created for guaranteeing the consistency of the flow coefficient predictions with respect to the number of cells. And it was found that the flow coefficient became independent of the mesh resolution when the number of cells reached 5.1 million, 4.5 million and 5.0 million cells for 25%, 50% and 75% prototypes, respectively; and 6.4 million, 4.9 million and 5.8 million cells for the gate valve at 25%, 50% and 75% openings, respectively.

In the comparison of flow coefficients obtained using different turbulence models, it turned out that, for prototypes, the realizable k–ε model produced lower estimates at all openings; for gate valve, the predicted flow coefficient was lower only for the case of 75% opening, whilst it was not sensitive to these two turbulence models for the other two cases. Another finding was that the predicted flow coefficients of prototypes were lower than the predictions in gate valves, indicating that, from the point of view of the dissipation characteristics, the two devices are not completely equivalent.

The simulations were also compared against data from experiments, which were carried out by other people in the context of the same research activity, showing non–negligible underestimation for prototypes, especially at large openings. The most plausible reason is believed to be the fact that, in the numerical simulations, the rounded edges of the prototypes were modeled as sharp edges, thereby resulting in higher dissipation. Conversely, the predictions of the gate valve showed better agreement, and the small deviations were interpreted as a result of having some chamfers removed during simulations.

The latter part of the thesis is focused on two–phase modeling and wear estimation on the prototypes. The sand particles were first tracked by the DPM model in Fluent, one–way coupling was selected as the volume fraction of sand being very low. Afterwards, semi–empirical models, namely E/CRC, DNV–GL15 and Oka et al. were chosen to make wear estimates, which were performed using an in–house code developed by the FluidLab research group after briefly exploring an embedded utility in Fluent. Firstly, the consistency study on number of parcels suggested that it was required to inject at least 50000 parcels. Regarding to the effects of number of computational cells, the results were similar to single–phase flow study.

Visual inspection of the eroded surface revealed that the most severe erosion occurs at the bottom of the pipe underneath the prototype and along its upstream dege.

A sensitivity analysis of the wear estimates with respect to the main sub–models and parameters of the computational model was carried out. The study of forces included in the particle equation of motion indicated that gravitational force and buoyancy, virtual mass force, lift force and pressure gradient force could not be neglected to have reliable estimates. Changing the restitution coefficients correlations would change the predicted integral erosion rate, with Forder correlations yielding a value between the predictions obtained by assuming perfectly elastic collisions and by employing the Grant & Tabakoff correlations, but the effect was not very significant. The investigation of the non spherical factor showed that the shape of the grains has influence, it was found that the round particles cause more erosion in this study, which might be a result of more impingement against the walls. Finally, the comparison among erosion models concluded that choosing different models could result in considerable difference in the wear predictions, up to one order of magnitude.

Currently, the erosion predictions of the gate valve is under investigation. It is suggested in this thesis that the prototypes allow good representation of the wear of the gate hole, but further geometries are needed to be developed to model the erosion of the valve chamber, which seems to have predominant contribution to the overall

mass loss. Immediate future development will be the simulation of gate valve erosion for different operating parameters, such as the type and diameter of the solid particles, the flow velocity and the loading of solids, in order to come up with some predictive formula for engineering use.

References

[1] *Ansys fluent theory guide*. Ansys, Inc., Canonsburg, PA 15317, USA, 15.0 edition, 2013.

[2] *Ansys fluent user guide*. Ansys, Inc., Canonsburg, PA 15317, USA, 15.0 edition, 2013.

[3] R.Jr. Bellman and A. Levy. Erosion mechanism in ductile metals. *Wear*, 70(1): 1–27, 1981.

[4] X. Chen, B.S. McLaury, and S.A. Siamack. Numerical and experimental investigation of the relative erosion severity between plugged tees and elbows in dilute gas/solid two-phase flow. *Wear*, 261(7):715–729, 2006.

[5] *DNVGL–RP–O501 Recommended Practice: Managing sand production and erosion*. DNVGL, Oslo, Norway, 2015.

[6] I. Finnie, A. Levy, and D.H. McFadden. Fundamental mechanisms of the erosive wear of ductile metals by solid particles. In *Erosion: Prevention and Useful Applications*. ASTM International, 1979.

[7] A. Forder, M. Thew, and D. Harrison. A numerical investigation of solid particle erosion experienced within oilfield control valves. *Wear*, 216(2):184–193, 1998.

[8] A. Haider and O. Levenspiel. Drag coefficient and terminal velocity of spherical and nonspherical particles. *Powder technology*, 58(1):63–70, 1989.

[9] K. Haugen, O. Kvernvold, A. Ronold, and R. Sandberg. Sand erosion of wear-resistant materials: Erosion in choke valves. *Wear*, 186–187:179–188, 1995.

[10] *Industrial–process control valves–Part 2–3: Flow capacity–Test procedures*. IEC, Geneva, Switzerland, 1997.

[11] K. Lien, J.P. Monty, M.S. Chong, and A. Ooi. The entrance length for fully developed turbulent channel flow. In *15th Australian Fluid Mechanics Conference*, volume 15, pages 356–363, 2004.

[12] Z. Lin, X.D. Ruan, Z.C. Zhu, and X. Fu. Three-dimensional numerical investigation of solid particle erosion in gate valves. *Proceedings of the Institution of Mechanical Engineers, Part C: Journal of Mechanical Engineering Science*, 228 (10):1670–1679, 2014.

[13] B.S. McLaury, J. Wang, S.A. Shirazi, J.R. Shadley, and E.F. Rybicki. Solid particle erosion in long radius elbows and straight pipes. In *Society of Petroleum Engineers*, number SPE–38842–MS, 1997.

[14] R. Mei. An approximate expression for the shear lift force on a spherical particle at finite reynolds number. *International Journal of Multiphase Flow*, 18(1):145–147, 1992.

[15] G.V. Messa and S. Malavasi. The effect of sub-models and parameterizations in the simulation of abrasive jet impingement tests. *Wear*, 370–371:59–72, 2016.

[16] D.O. Njobuenwu and M. Fairweather. Modelling of pipe bend erosion by dilute particle suspensions. *Computers & Chemical Engineering*, 42:235–247, 2012.

[17] L. Nøkleberg and T. Søntvedt. Erosion of oil&gas industry choke valves using computational fluid dynamics and experiment. *International Journal of Heat and Fluid Flow*, 19(6):636–643, 1998.

[18] Y.I. Oka and T. Yoshida. Practical estimation of erosion damage caused by solid particle impact: Part 2: Mechanical properties of materials directly associated with erosion damage. *Wear*, 259(1–6):102–109, 2005.

[19] Y.I. Oka, K. Okamura, and T. Yoshida. Practical estimation of erosion damage caused by solid particle impact: Part 1: Effects of impact parameters on a predictive equation. *Wear*, 259(1–6):95–101, 2005.

[20] R. Paggiaro, J.D. Friedemann, E. Gharaibah, and Y. Zhang. Prediction of sand erosion in choke valves–cfd model development and validation against experiments. In *Offshore Technology Conference*, number OTC–24271–MS, 2013.

[21] M. Parsi, K. Najmi, F. Najafifard, S. Hassani, B.S. McLaury, and S.A. Shirazi. A comprehensive review of solid particle erosion modeling for oil and gas wells

and pipelines applications. *Journal of Natural Gas Science and Engineering*, 21: 850–873, 2014.

[22] H. Schlichting. *Boundary Layer Theory*. McGraw–Hill, New York, 1960.

[23] C. Stelian. Analysis of turbulent flow in closed and open channels with application in electromagnetic velocimetry. *Magnetohydrodynamics*, 48(4):637–649, 2012.

[24] M.S. Wallace, W.M. Dempster, T. Scanlon, J. Peters, and S. McCulloch. Prediction of impact erosion in valve geometries. *Wear*, 256(9–10):927–936, 2004.

[25] D.W. Wheeler and R.J.K. Wood. Erosion of hard surface coatings for use in offshore gate valves. *Wear*, 258(1–4):526–536, 2005.

[26] F.M. White. *Fluid Mechanics*. McGraw–Hill Higher Education, New York, 4th edition, 1998.

[27] C.Y. Wong, C. Solnordal, A. Swallow, S. Wang, L. Graham, and J. Wu. Predicting the material loss around a hole due to sand erosion. *Wear*, 276–277:1–15, 2012.

[28] R.J.K. Wood, T.F. Jones, J. Ganeshalingam, and N.J. Miles. Comparison of predicted and experimental erosion estimates in slurry ducts. *Wear*, 256(9–10): 937–947, 2004.

[29] Y. Zhang, E.P. Reuterfors, B.S. McLaury, S.A. Shirazi, and E.F. Rybicki. Comparison of computed and measured particle velocities and erosion in water and air flows. *Wear*, 263(1–6):330–338, 2007.